1-1-2016

Fatigue Behavior of Ti-6Al-4V ELI including Mean Stress Effects

Patricio E. Carrion

Fatigue behavior of Ti-6Al-4V ELI including mean stress effects

By

Patricio E. Carrion

A Thesis
Submitted to the Faculty of
Mississippi State University
in Partial Fulfillment of the Requirements
for the Degree of Master of Science
in Mechanical Engineering
in the Department of Mechanical Engineering

Mississippi State, Mississippi

December 2016

Fatigue behavior of Ti-6Al-4V ELI including mean stress effects

By

Patricio E. Carrion

Approved:

_____

Nima Shamsaei
(Major Professor)

_____

Steven R. Daniewicz
(Committee Member)

_____

Andrew L. Oppedal
(Committee Member)

_____

Jutima Simsiriwong
(Committee Member)

_____

Yucheng Liu
(Graduate Coordinator)

_____

Jason Keith
Dean
Bagley College of Engineering

Name: Patricio E. Carrion

Date of Degree: December 9, 2016

Institution: Mississippi State University

Major Field: Mechanical Engineering

Major Professor: Nima Shamsaei

Title of Study: Fatigue behavior of Ti-6Al-4V ELI including mean stress effects

Pages in Study 67

Candidate for Degree of Master of Science

This study investigates the cyclic deformation, fatigue behavior, and failure mechanisms for Ti-6Al-4V ELI (extra low interstitial) with and without mean strain/stress. Mean stress effects on fatigue behavior were studied using four strain ratios. Fatigue data generated was used to assess mean stress fatigue life prediction approaches, including stress-based methods such as Goodman, Gerber, Morrow, Walker and Kwofie; as well as strain-based models, such as Morrow, Smith-Watson-Topper, Walker, Kwofie, Ince-Glinka and a modified version of the Smith-Watson-Topper. The stress-based models did not yield reasonable results and data scatter was observed. The strain-based models offered better results, specifically the Morrow approach which provided more accurate fatigue life predictions. Fractography analysis determined that the influence of material defects on fatigue life had no major differences across all the strain ratios considered. Overall observations indicate that inclusions near the surface had great influence on the fatigue behavior.

Keywords: Fatigue; Cyclic Deformation; Mean Stress Models; Life Predictions; Damage Mechanisms; Titanium

DEDICATION

I would like to dedicate this research to my beloved family, Jorge Delgado, Maribel Delgado, Josue Carrion, Andres Carrion and Ayleen Delgado. Thank you for all your support and encouragement, you all provided me with strength and will to accomplish my goals.

ACKNOWLEDGEMENTS

The author would like to express his upmost gratitude to all of the people whose assistance made this thesis possible. First, the most sincere thanks to Dr. Nima Shamsaei, my mentor and advisor, for his time, effort, persistence, and guidance throughout all the challenges that were faced in the process. The author will also like to extend his appreciation to the other members of the committee, Dr. Steven R. Daniewicz, Dr. Andrew L. Oppedal, and Dr. Jutima Simsiriwong, for the mentoring offered, as well as all the people at the Center for Advanced Vehicular Systems (CAVS) for their help and support.

This effort was sponsored by the Engineering Research and Development Center under Cooperative Agreement number W912HZ-15-2-0004. The views and conclusions contained herein are those of the authors and should not be interpreted as necessarily representing the official policies or endorsements, either expressed or implied, of the Engineering Research and Development Center or the U.S. Government.

TABLE OF CONTENTS

LIST OF TABLES

LIST OF FIGURES

NOMENCLATURE

$2N_f$	number of reversals to failure
$2N_k$	Kwofie equivalent reversals to failure
$2N_w$	Walker equivalent reversals to failure
b	fatigue strength exponent
b_σ	stress-based fatigue strength exponent
c	fatigue ductility exponent
E	modulus of elasticity
E'	cyclic modulus of elasticity
$\%\ EL$	percent elongation
GS	ASTM grain size number
K'	cyclic strength coefficient
n'	cyclic strength exponent
N	number of cycles
N_f	number of cycles to failure
$\%RA$	percent reduction of area
R_ε	strain ratio $(\varepsilon_{min}/\varepsilon_{max})$
R_σ	stress ratio $(\sigma_{min}/\sigma_{max})$
α	mean stress sensitivity parameter

$\frac{\Delta\varepsilon}{2}$, ε_a	strain amplitude
$\frac{\Delta\varepsilon_e}{2}$	elastic strain amplitude
$\frac{\Delta\varepsilon_p}{2}$	plastic strain amplitude
$\frac{\Delta\sigma}{2}$, σ_a	stress amplitude
ε_f	true fracture strain
ε'_f	fatigue ductility coefficient
ε_{max}	maximum strain
ε_{min}	minimum strain
γ	Walker fitting constant
σ_{ar}	equivalent stress amplitude
σ'_f	fatigue strength coefficient
$\sigma'_{f,\sigma}$	stress-based fatigue strength coefficient
$\tilde{\sigma}_{fB}$	true fracture strength, corrected
σ_m	mean stress
σ_{max}	maximum stress
σ_{min}	minimum stress
σ_u	ultimate tensile strength
σ_y	yield strength

CHAPTER I

INTRODUCTION

Titanium alloys are used in a wide range of industrial applications because of their excellent combination of mechanical and chemical properties. Titanium alloys have a relatively high strength to weight ratio, low density, easy formability, corrosion resistance, microstructural stability and acceptable performance at elevated temperatures (300-600 °C) [1–3]. The high strength, low density, bio-compatibility, and good formability characteristics of titanium are desirable for biomedical applications [3–5]. In the biomedical field there have been extensive studies regarding the implementation of titanium (Ti-6Al-4V ELI specifically) in dental implants, heart valves, bone and joint implants, as well as in the manufacturing of several components used in the reattachment of fractured bones [4–7].

Mechanical properties of titanium alloys depend substantially on the microstructure, including the phases present (α or β), and the grain size and shape which are formed during the manufacturing and heat treatment processes. An understanding of the different types of microstructures and their advantages is necessary to carefully choose the type of alloy that offers the best performance for a given application [1]. Ti-6Al-4V is the most widely used among the different types of titanium alloys. Ti-6-Al-4V is an α+ β type alloy that can be obtained with any of the three types of microstructure attributed to titanium (i.e. equiaxed, lamellar or bimodal), depending on the material

processing and heat treatment applied. Ti-6Al-4V has balanced strength and toughness as well as workability and weldability. The latter property has made Ti-6AL-4V a great candidate for the additive manufacturing process [8], which provides the ability to fabricate customized parts with complex geometries, such as bio-implants. Ti-6Al-4V, particularly Ti-6Al-4V ELI (extra low interstitial) with low impurity levels of O, Fe, N, and C, is used as a metallic biomaterial because of its excellent corrosion resistance and biocompatibility. This particular titanium alloy was the first to be registered as a biomaterial [6,9,10] and has its own dedicated ASTM standard (F136) [11]. One application of Ti-6Al-4V as a biomaterial is for failed hard tissue, where failure due to fatigue is of great concern, as these implants have irregular shapes and are under asymmetric cyclic loading, thus resulting in the presence of mean stress. Damage may be caused by variable and complex loading conditions, resulting in plastic deformation at the microscopic level. As an example, a hip joint implant is exposed to loads caused by physical activities like running, jumping or walking. Such activities cause cyclic loading and in some cases periodic overloading [4,5,12].

In this study, Ti-6Al-4V ELI with fully equiaxed grain structure is investigated. The equiaxed structure is chosen because it possesses a high fatigue strength when compared to other microstructures [13,14], while there are other studies indicating the bimodal or lamellar microstructure have better fatigue properties [13,15]. The vast majority of fatigue research regarding Ti-6Al-4V has focused on fatigue crack growth and the stress-life approach, primarily in the high cycle fatigue regime [4–6,12,15]. Here, we employ the strain-life approach because some of the components made for biomedical applications are not only subjected to cyclic loading but also, in some cases, periodical

overloading due to body movements, resulting in local plastic deformation [4,12]. The strain-life approach was selected because it offers a localized measurement of strain, and it has been proven to correlate low cycle fatigue data in a better manner than the stress-life approach [16].

Mean stress effects on fatigue behavior of Ti-6Al-4V ELI were also studied in this research. While one can prevent mean stress from affecting the fatigue life of the material during testing, for example using fully-reversed fatigue testing in load-controlled condition, mean stresses may be present in many industrial applications, specifically under variable amplitude loading [16,17]. Different mean stress effects can occur; among the most common are ratcheting (during load-controlled testing) and mean stress relaxation (during strain-controlled testing). Plastic deformation is attributed to be the cause of mean stress relaxation, meaning that the amount of relaxation depends on the strain amplitude. In strain-controlled cyclic loading with mean strain, although mean stress will be present initially, it may fully or partially relax as cyclic loading progresses. It is known that tensile mean stresses reduce the fatigue life and compressive mean stresses are neutral, if not beneficial; therefore, the effects of mean strain/stress need to be taken into consideration [16]. There are many models used to account for mean stress effects on fatigue behavior. In this study, the Goodman, Gerber, Morrow, Walker and Kwofie mean stress methods are considered to model the stress-life behavior. For the strain-life approach with mean stress effects, Morrow's parameter, the Smith-Watson-Topper equation (SWT), the Walker method, the Kwofie exponential stress function, the Ince-Glinka model and a Modified Smith-Watson-Topper (MSWT) equation are investigated.

CHAPTER II

EXPERIMENTAL PROGRAM

Material and Specimen

Ti-6Al-4V ELI, mill annealed wrought hot rolled bar was utilized in this study. Table 2.1 displays the chemical composition of this alloy based on the manufacturer supplied data. The original diameter of the provided bars was 12.7 mm. The bars were annealed at 1300 °F for 1 hour and air cooled. Tension and fatigue specimens were manufactured from the 12.7 mm round bars in the longitudinal direction. Each bar was sectioned into 165 mm long rods and then machined into round specimens with the dimensions and geometry specified in Figure 2.1, based on ASTM standard E606/E606M-12 [18]. To conduct strain-controlled cyclic tests, the specimens had a uniform gage section to allow for the use of an extensometer. Before testing was performed, each specimen was polished to a 0.5 μm surface finish, thus eliminating machining marks and creating polishing marks in the longitudinal direction of the specimen. The polished surfaces were later examined under an optical microscope to ensure that there were no polishing marks in any direction other than the longitudinal (direction of the applied force). Per suggestion of ASTM standard E606 [18], all specimens were subjected to an acrylic application on the gage section (at two points) in order to protect the polished surface from the blades of the extensometer used to measure the strain.

Experimental Procedures

Analysis of Ti-6Al-4V ELI started first with an investigation of the microstructural characteristics from the wrought mill annealed bar. Segments were dissected, and cross sections in both the longitudinal and radial directions were used to capture images. Both samples were etched using a solution consisting of 2 mL of hydrofluoric acid diluted in 98 mL of distilled water. The ASTM standard E112-13 [19] was followed to determine the average grain size. Figure 2.2(a) illustrates the orientation of the dissected segments. An optical microscope was used to capture the images seen in Figure 2.2(b) and 2.2(c), which present the etched microstructure indicating the grain boundaries with the equiaxed α phase. Figure 2.2(b) presents the radial direction view and Figure 2.2(c) presents the longitudinal direction view. A scanning electron microscope (SEM) was also used to observe the microstructure in the radial direction, presented in Figure 2.2(d), as a way of comparing the findings to SEM images found in the literature [1–3,9,13,15]. It can be seen from Figure 2.2(d) that the etchant corroded the α grains, leaving the β phase. Rather than the clear view of the grain boundaries that Figure 2.2(b) and 2.2(c) provide, there is no indication of boundaries between α grains in Figure 2.2(d), giving a clear view of the distribution of the β phase. After careful measurements, the α grain size number was determined to be GS = 13, which has an average diameter of 4 μm.

Strain-controlled monotonic tension tests were carried out per ASTM E8 [20] standard at a strain rate of 0.001 s^{-1}, to determine mechanical properties including yield strength, σ_y, ultimate tensile strength, σ_u, percent elongation, *%EL*, and percent area

reduction, *%RA*. After testing, the specimen cross section at final fracture was examined, and the reduction in area was measured.

Fatigue properties were generated by conducting strain-controlled fatigue tests with and without mean strains. The strain ratio, R_ε, is defined by Eq. (2.1),

$$R_\varepsilon = \frac{\varepsilon_{min}}{\varepsilon_{max}} \tag{2.1}$$

where ε_{min} is the minimum strain and ε_{max} is the maximum strain. The R_ε values used in study were -1 (fully-reversed), -0.5 (tension-compression), 0 (tension-release) and 0.5 (tension-tension). A schematic of the type of loading of each R_ε value is illustrated in Figure 2.3. As previously mentioned, strain-controlled testing may result in some mean stresses; thus, the stress ratio (i.e. R_σ) was also calculated for all tests as $\sigma_{min}/\sigma_{max}$. Table 2.2 offers a compilation of the various tests and parameters used as well as results from the testing procedure, including strain ratio, R_ε, first cycle modulus of elasticity, E, strain amplitude, ε_a, and the respective elastic, $\Delta\varepsilon_e/2$, and plastic, $\Delta\varepsilon_p/2$, strain amplitude components, stress amplitude, σ_a, and mean stress, σ_m, at mid-life stable cycle, stress ratio, R_σ, and the number of reversals to failure, $2N_f$. The raw data collected and used in this study can be found in [21]. The frequency during testing was adjusted according to the strain amplitude: the higher the amplitude, the slower the frequency to generate a nearly constant average strain rate for all fatigue tests. For each strain amplitude, a minimum of two specimens were tested to ensure that the test data was consistent and could be replicated.

Strain-controlled fatigue experiments were conducted at room temperature in ambient air using a tapered sinusoidal strain waveform. The strain amplitudes varied

from 0.0015 to 0.0120 mm/mm, and the frequency ranged between 0.5 and 5 Hz. In order to increase the frequency in some cases, once the cyclic behavior stabilized, the strain-controlled mode was switched to load-controlled, and the extensometer was removed. The control mode was changed only for tests in which there was only elastic deformation and the stress and strain response was the same in either the load-controlled or strain-controlled condition. Any experiment that reached over 1.0E6 cycles was stopped and determined to be a runout. Upon fatigue test completion, the fracture surface was examined using a scanning electron microscope (SEM). Fractography analysis was performed on one fracture surface from each broken specimen. If needed, the other surface was inspected as well. Each surface was compared and analyzed to find distinct crack initiation sites and regions associated with fatigue crack propagation.

Table 2.1 Chemical composition of Ti-6Al-4V ELI used in this study.

Element	**Al**	**C**	**Fe**	**N**	**O**	**V**	**Y**	**Ti**
Wt%	6.12	0.013	0.190	0.004	0.120	3.99	<0.005	BAL

Table 2.2 Summary of constant amplitude strain-controlled fatigue tests for Ti-6Al-4V ELI under fully-reversed and mean strain conditions.

R_ε	E	ε_a	$\Delta\varepsilon_p/2$	$\Delta\varepsilon_e/2$	σ_a	σ_m	R_σ	$2N_f$
	GPa	mm/mm	mm/mm	mm/mm	MPa	MPa		reversals
Fully-Reversed Tests								
-1	107	0.0120	0.0045	0.0075	698	13	-0.96	2,202
-1	108	0.0120	0.0045	0.0075	729	-6	-1.02	2,336
-1	105	0.0120	0.0042	0.0078	710	18	-0.95	3,164
-1	107	0.0100	0.0026	0.0074	718	23	-0.94	3,760
-1	105	0.0100	0.0028	0.0072	703	-5	-1.02	3,986
-1	105	0.0100	0.0025	0.0075	705	23	-0.94	4,540
-1	106	0.0080	0.0010	0.0070	695	-18	-1.05	12,914
-1	108	0.0080	0.0009	0.0071	713	-23	-1.07	14,338
-1	106	0.0070	0.0000	0.0070	748	11	-0.97	49,174
-1	106	0.0070	0.0000	0.0070	746	15	-0.96	49,812
-1	108	0.0060	0.0000	0.0060	653	25	-0.93	124,952
-1	105	0.0060	0.0000	0.0060	648	-4	-1.01	128,050
-1	105	0.0060	0.0000	0.0060	652	11	-0.97	207,610
-1	107	0.0050	0.0000	0.0050	551	3	-0.99	>2,713,156
-1	105	0.0040	0.0000	0.0040	418	26	-0.88	>2,337,270
-1	107	0.0040	0.0000	0.0040	433	24	-0.89	>4,431,694
Mean Strain Tests								
-0.5	106	0.0090	0.0021	0.0069	729	48	-0.88	10,516
-0.5	107	0.0090	0.0022	0.0068	735	44	-0.89	11,546
-0.5	106	0.0075	0.0008	0.0067	714	78	-0.80	22,700
-0.5	107	0.0075	0.0006	0.0069	733	70	-0.83	22,992
-0.5	106	0.0060	0.0001	0.0059	653	174	-0.58	128,248
-0.5	107	0.0045	0.0000	0.0045	485	92	-0.68	>2,371,298
0	107	0.0100	0.0024	0.0076	733	45	-0.88	5,464
0	105	0.0100	0.0023	0.0077	729	50	-0.87	6,724
0	103	0.0080	0.0015	0.0065	671	178	-0.58	11,398
0	105	0.0080	0.0014	0.0066	690	71	-0.81	13,992
0	105	0.0060	0.0002	0.0058	615	216	-0.48	57,292
0	106	0.0060	0.0002	0.0058	616	222	-0.47	65,472
0	107	0.0040	0.0001	0.0039	422	401	-0.03	>2,506,668
0.5	105	0.0045	0.0000	0.0045	445	461	0.02	64,066

Table 2.2 (continued)

0.5	107	0.0045	0.0000	0.0045	456	408	-0.06	98,788
0.5	106	0.0040	0.0000	0.0040	401	521	0.13	129,922
0.5	105	0.0040	0.0000	0.0040	401	482	0.09	230,884
0.5	107	0.0030	0.0000	0.0030	304	582	0.31	>2,104,496
0.5	107	0.0030	0.0000	0.0030	308	574	0.30	>2,370,558
0.5	104	0.0025	0.0000	0.0025	251	697	0.47	>2,319,500
0.5	109	0.0020	0.0000	0.0020	205	660	0.53	>2,047,510
0.5	108	0.0015	0.0000	0.0015	157	730	0.65	>2,048,000

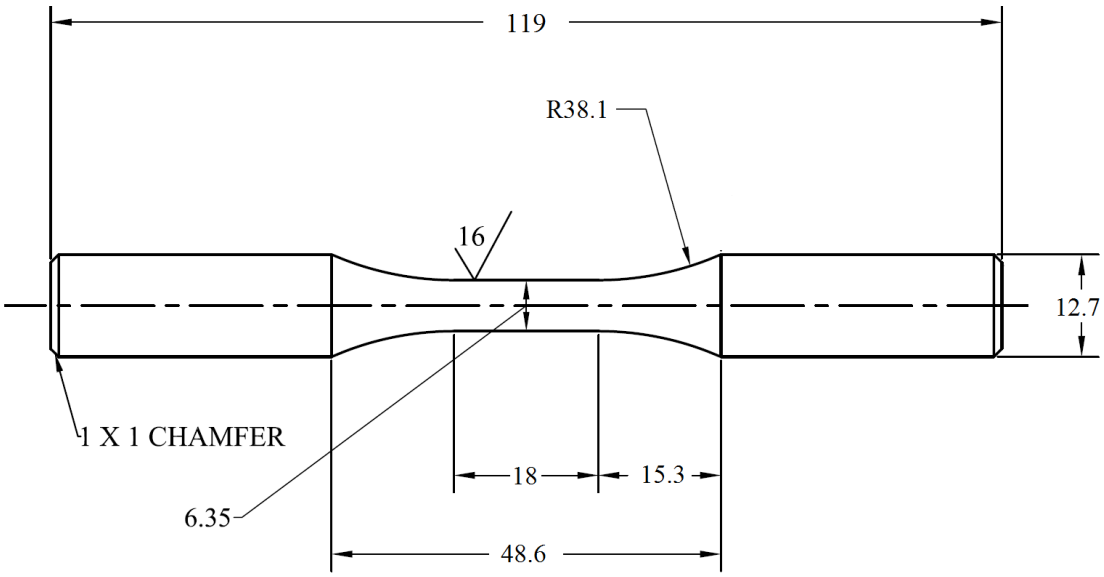

Figure 2.1 Round fatigue specimen with uniform gage section per ASTM standard E606/E606M-12 used in this study [18,21].

NOTE: All dimensions are in mm

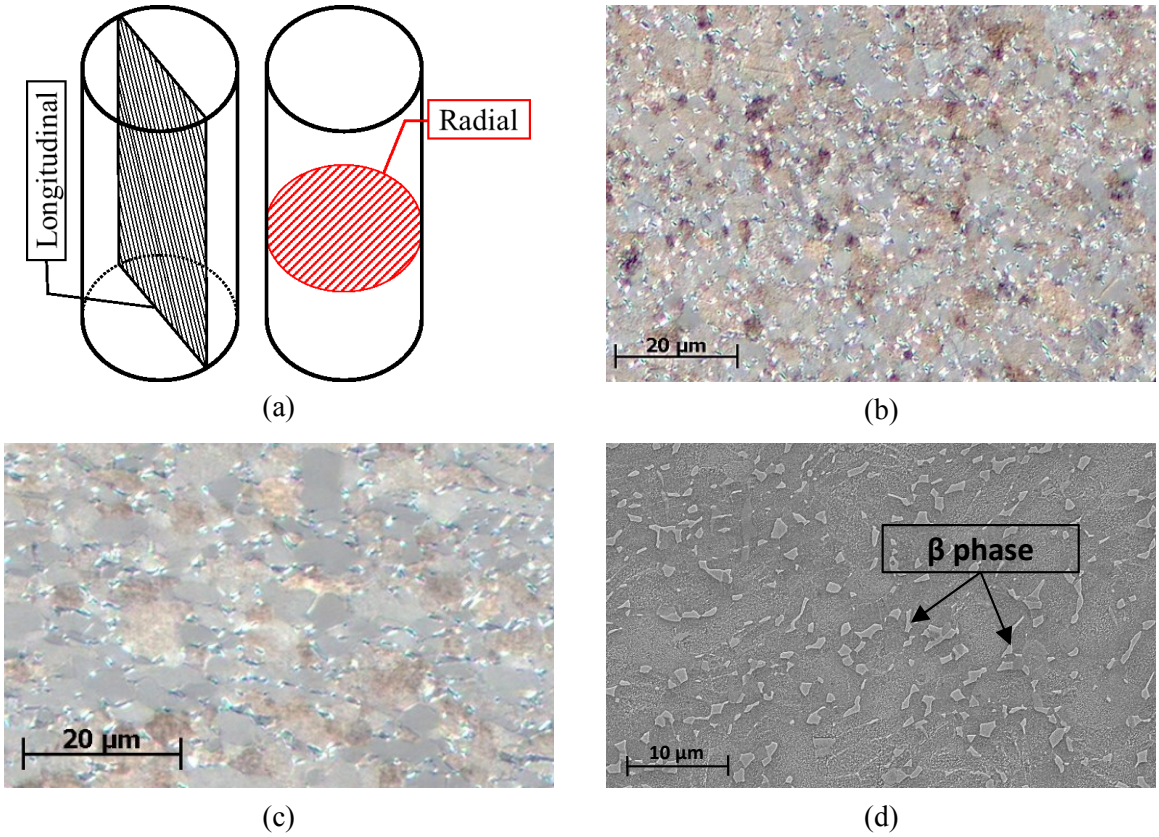

Figure 2.2 Microstructure images revealing different orientation of the equiaxed α grains of Ti-6Al-4V ELI used in this study.

(a) Schematic showing the orientation planes of the dissected segments. Optical microscopy images in (b) radial, and (c) longitudinal planes. (d) Radial SEM image showing the β phase in the Ti-6Al-4V ELI specimen.

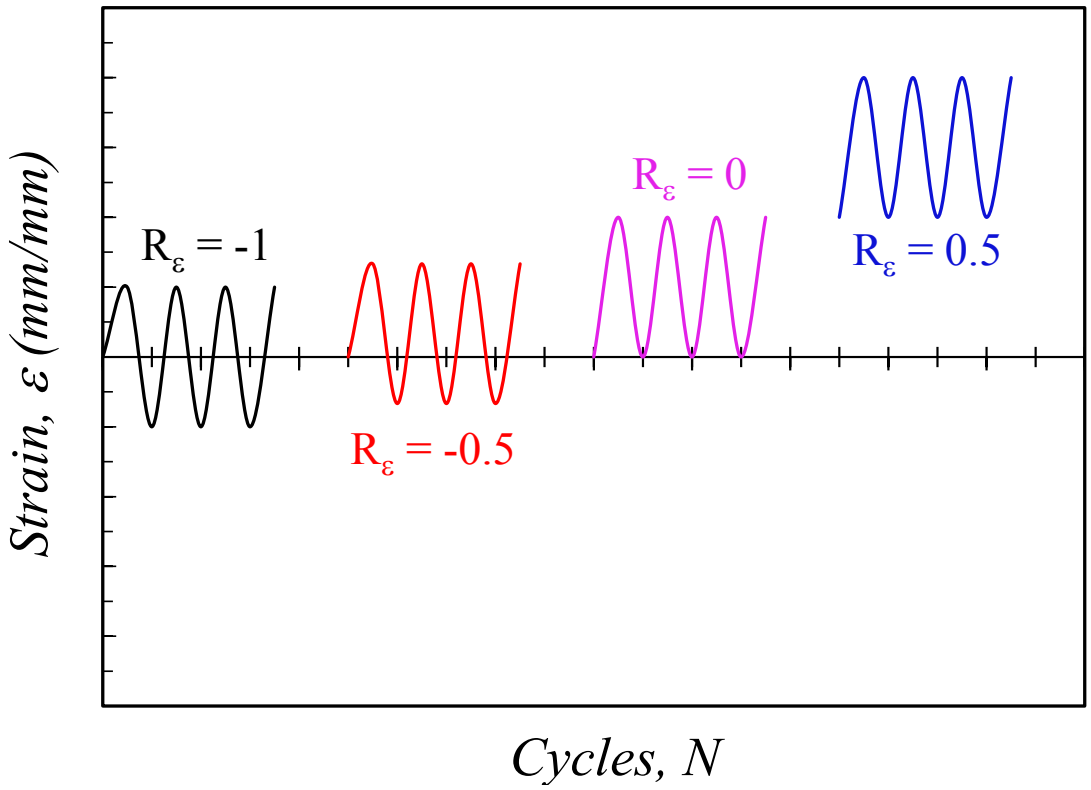

Figure 2.3 Schematic of the R_ε values used in study.

This includes -1 (fully-reversed), -0.5 (tension-compression), 0 (tension-release) and 0.5 (tension-tension).

CHAPTER III

EXPERIMENTAL RESULTS

Monotonic and Cyclic Deformation

The monotonic tensile stress-strain curve for Ti-6Al-4V ELI is presented in Figure 3.1 by both the engineering and true stress-strain curves. Table 3.1 lists the monotonic mechanical properties determined by the tensile tests using the engineering stress and strain, including modulus of elasticity, E, yield strength, σ_y, ultimate tensile strength, σ_u, elongation to failure, $\%EL$, percent reduction of area, $\%RA$, true fracture strength, $\tilde{\sigma}_{fB}$, and true fracture strain, ε_f. As can be seen from the engineering stress-strain curve in Figure 3.1, the material exhibits very limited strain hardening; once the strain reached a value of 0.0100 mm/mm, permanent plastic deformation is present and the stress changes little as the strain increases until final fracture.

The cyclic deformation behavior of Ti-6Al-4V ELI and the respective cyclic deformation properties were obtained from stress-strain responses under fully-reversed axial loading (i.e. R_ε= -1). Seven different strain amplitudes were used to characterize the cyclic deformation behavior of the material. These strains were selected in order to provide a representation of both fully elastic and elastic-plastic cyclic deformation. The cyclic stress-strain curve, with the use of the Ramberg-Osgood relationship based on the stabilized mid-life hysteresis loops was obtained. The cyclic strength coefficient, K', and strain hardening exponent, n', were calculated using linear regression analysis of the mid-

life steady state stress amplitude, σ_a, versus the plastic strain amplitude, $\Delta\varepsilon_p/2$, of the fully-reversed cyclic data in the log-log scale, based on Eq. (3.1). Using the Ramberg-Osgood relationship the cyclic stress-strain behavior can then be expressed based on Eq. (3.2).

$$\sigma_a = K'\left(\frac{\Delta\varepsilon_p}{2}\right)^{n'} \tag{3.1}$$

$$\varepsilon_a = \frac{\Delta\varepsilon_e}{2} + \frac{\Delta\varepsilon_p}{2} = \frac{\sigma_a}{E} + \left(\frac{\sigma_a}{K'}\right)^{\frac{1}{n'}} \tag{3.2}$$

where the strain amplitude, ε_a, is equal to the sum of the elastic strain amplitude, $\Delta\varepsilon_e/2$, and the plastic strain amplitude $\Delta\varepsilon_p/2$. The cyclic deformation properties obtained for Eq. (3.2) are listed in Table 3.1. The resulting Ramberg-Osgood relationship for Ti-6Al-4V ELI in this study is presented in Figure 3.2, superimposed with the fully-reversed cyclic stress-strain data and engineering monotonic stress-strain curve. The cyclic stress-strain curve is below the monotonic curve, an indication of cyclic softening behavior for Ti-6Al-4V ELI. Cyclic softening behavior has been also reported in these dual-phase titanium alloys elsewhere [5,14]. However, no cyclic softening or hardening has been observed for pure titanium and some other titanium alloys [17,22].

A nearly stable plateau stress behavior after the initial elastic region can be observed in Figure 3.2 for Ti-6AL-4V ELI. At strains above 0.0070 mm/mm, there was a stabilization of stress amplitude values, and the stress exhibited little change as the strain amplitude increased, staying within a range of 695 MPa to 748 MPa. For example, at 0.0120 mm/mm strain amplitude, the largest alternating stress was 729 MPa, while at a strain amplitude of 0.0080 mm/mm the smallest stress amplitude was 713 MPa. For 0.0040, 0.0050, 0.0060 and 0.0070 mm/mm strain amplitudes, the cyclic data points fell

along the elastic region of the monotonic curve. One can also observe from Figure 3.2 that the Ramberg-Osgood relation cannot account for the fully elastic behavior at strain amplitude of 0.0070 mm/mm as it predicts the presence of plastic strain at this strain level. The cyclic response at 0.0070 mm/mm strain amplitude showed no softening but instead was stable and had a constant stress of 750 MPa; this stress is higher than the stable cycle stresses found at higher strains, meaning that cyclic softening only occurs when plastic strain is present.

Figure 3.3 illustrates the mid-life stable hysteresis loops for the fully-reversed fatigue data. As can be seen from this figure, the strain is predominantly elastic, and plastic strain is negligible for strain amplitudes of 0.0040, 0.0050, 0.0060 and 0.0070 mm/mm. A plastic strain value less than 0.0001 mm/mm was considered to be negligible in this study. For the higher strain amplitude values of 0.0080, 0.0100 and 0.0120 mm/mm, the presence of plastic strain was noted, as seen in Figure 3.3. In conjunction with this observation, it was also found that the elastic component of these strain amplitudes reached a maximum value ranging from 0.0070 to 0.0075 mm/mm. Figure 3.3 also illustrates how there is no further increase in stress with an increase in strain amplitude, but rather a slight decrease. The decrease in stress for strain amplitudes of 0.0120, 0.0100, and 0.0080 mm/mm, where plastic strain is present, is attributed to cyclic softening. It was also observed that for all the previously mentioned strain amplitudes, the stress reduced to approximately 700 MPa. At strain amplitudes of 0.0070 mm/mm and lower, the stress response was stable and fully elastic; therefore, cyclic softening was not present.

The mean stress responses during mean strain testing with different R_ε values are presented in Figure 3.4, where the mean stress values versus the number of cycles are plotted. When testing at R_ε = -0.5, presented in Figure 3.4(a), the following strain amplitudes were considered: 0.0045, 0.0060, 0.0075, and 0.0090 mm/mm. The mean stress response at the strain amplitude of 0.0045 mm/mm with R_ε = -0.5 did not exhibit any relaxation and was constant through the entire test. The mean stress response of 0.0060 mm/mm strain amplitude with R_ε = -0.5 exhibited relaxation to 172 MPa. Even without full mean stress relaxation, the fatigue life at R_ε = -0.5 was similar to the one observed for R_ε = -1 at the same strain amplitude. The mean stress response of 0.0075 mm/mm strain amplitude with R_ε = -0.5 indicated relaxation to 78 MPa, suggesting that even with a minimal presence of plastic deformation (see Table 2.2), relaxation may occur. As strain amplitude increased to 0.0090 mm/mm with the same R_ε = -0.5, almost full mean stress relaxation was observed.

For R_ε = 0, shown in Figure 3.4(b), mean stress relaxation was observed for all tests, although the relaxation at 0.0040 mm/mm strain amplitude was not substantial. For 0.0040 mm/mm strain amplitude, the mean stress was over 400 MPa, and while very minor stress relaxation was present, the fatigue life was infinite, and thus, unaffected when compared to the fully-reversed test with the same strain amplitude. When the strain amplitude of 0.0060 mm/mm with R_ε = 0 was applied, mean stress relaxation was observed, although not to its full extend. The fatigue life of 0.0060 mm/mm strain amplitude with R_ε = 0 was also reduced as compared to the R_ε = -1 test at the same strain amplitude. The fatigue lives of 0.0060 mm/mm strain amplitude with R_ε = -1 ranged from

124,952 to 207,610 reversals, while the longest fatigue life was 65,472 reversals for R_ε = 0. At 0.0080 mm/mm strain amplitude with R_ε = 0, almost full mean stress relaxation was observed; thus, the cycles to failure and the stress response were not different of the ones obtained from the test at 0.0080 mm/mm strain amplitude with R_ε = -1. Similar behavior was observed at 0.0100 mm/mm strain amplitude; mean stress showed almost full relaxation, and no effect on the fatigue life was observed when compared to fully-reversed fatigue tests at the same strain level. Therefore, one may conclude that mean strain may not affect fatigue behavior of Ti-6AL-4V ELI when full mean stress relaxation occurs.

For R_ε = 0.5, the mean stress response was different than the previous R_ε values. The strain amplitudes considered for R_ε = 0.5 were 0.0015, 0.0020, 0.0025, 0.0030, 0.0040, and 0.0045 mm/mm. The stress amplitude responses of tests with R_ε = 0.5 were observed not to have any type of hardening or softening while the mean stress constantly reduced throughout the test period. As seen in Figure 3.4(c) for strain amplitudes of 0.0030, 0.0040, and 0.0045 mm/mm, the mean stress demonstrated continuous reduction, but not fully relaxed. The fatigue lives at strain amplitudes of 0.0045, and 0.0040 mm/mm, which were found to be runouts (i.e. over 1.0E6 cycles) for R_ε = -1, -0.5 and 0 cases, were reduced to finite lives. For example, the fatigue life at strain amplitude of 0.0040 mm/mm was greater than 1.0E6 cycles for R_ε = -1, while for R_ε = 0.5 at the same strain amplitude, the life did not surpass 230,884 reversals. This indicates the severe detrimental effect of a positive R_ε value on fatigue behavior, as it results in the presence of some considerable tensile mean stress.

In conclusion, the stress amplitude behavior for fully-reversed tests demonstrated that cyclic softening was present exclusively in strain amplitudes higher than 0.0070 mm/mm (as seen in Figure 3.3), where some plastic deformation existed. The effect of tensile mean strain was observed to be detrimental on the fatigue behavior of Ti-6Al-4V ELI when full mean stress relaxation did not occur and some tensile mean stress was present.

Fatigue Behavior

Figure 3.5 presents a semi-log plot of the stress amplitude, σ_a, versus reversals to failure, $2N_f$, for the fully-reversed strain-controlled fatigue tests generated in this study. It can be seen from this figure that at lives less than 20,000 reversals, which correspond to strain amplitudes ranging from 0.0120 to 0.0080 mm/mm, the stress amplitude stays relatively constant. There is little change in this range, and the stress amplitude is relatively flat within a range of 695 MPa to 734 MPa. The stress amplitude for lives longer than 100,000 reversals (i.e. 0.0060 to 0.0040 mm/mm strain amplitudes) decreases with a reduction in the strain amplitude. The only exception is the data points corresponding to 0.0070 mm/mm strain amplitude. As previously shown in Figure 3.2, there is no difference between the monotonic and cyclic stress response at this strain level, causing the stress response to be higher and stay at a constant stress amplitude. Specimens at higher strains, however, experience cyclic softening, resulting in a decreased stress response. This is the reason why these specimens exhibit a smaller stress response as compared to that of 0.0070 mm/mm strain amplitude, which is the highest fully elastic strain-controlled test in this study. Due to this type of behavior in strain-controlled fatigue tests, the stress-life plot in Figure 3.5 presents a significant amount of

scatter. Stress-life fatigue properties generated from the best fit to stress amplitude, σ_a, versus reversals to failure, $2N_f$, are listed in Table 3.1, including the stress-based fatigue strength coefficient, $\sigma'_{f,\sigma}$, and stress-based fatigue strength exponent, b_σ.

The Coffin-Mason model was implemented using the fully-reversed fatigue data to characterize the strain-life behavior which includes the plastic and elastic fatigue properties. Coffin-Mason is defined as the strain amplitude being equal to the sum of the elastic and plastic strain amplitudes. Mid-life stable hysteresis loops were used to find the stress amplitude, σ_a, and elastic strain amplitude, $\Delta\varepsilon_e/2$, allowing for the calculation of the plastic strain amplitude, $\Delta\varepsilon_p/2$, by subtracting the elastic strain amplitude from the total strain amplitude. The elastic component is given by Eq. (3.3), where the fatigue strength coefficient, σ'_f, and fatigue strength exponent, b, were obtained using linear regression on the log-log scale plot of the elastic strain amplitude, $\Delta\varepsilon_e/2$, versus reversals to failure, $2N_f$, data. The plastic component is given by Eq. (3.4), where the fatigue ductility coefficient, ε'_f, and the fatigue ductility exponent, c, were obtained using linear regression on the log-log scale plots of plastic strain amplitude, $\Delta\varepsilon_p/2$, versus reversals to failure, $2N_f$, data. Finally, Eq. (3.5) represents the total strain amplitude relation with reversals to failure.

$$\frac{\Delta\varepsilon_e}{2} = \frac{\sigma'_f}{E}\left(2N_f\right)^b \tag{3.3}$$

$$\frac{\Delta\varepsilon_p}{2} = \varepsilon'_f\left(2N_f\right)^c \tag{3.4}$$

$$\varepsilon_a = \frac{\Delta\varepsilon_e}{2} + \frac{\Delta\varepsilon_p}{2} = \frac{\sigma'_f}{E}\left(2N_f\right)^b + \varepsilon'_f\left(2N_f\right)^c \tag{3.5}$$

Strain-life fatigue properties for fully-reversed data are listed in Table 3.1. Note that $\sigma'_{f,\sigma}$ and b_σ were determined from the measured stress amplitude response versus

reversals to failure (see Figure 3.5), while σ'_f and b were determined from the resultant elastic strains amplitudes. Figure 3.6 illustrates the total, elastic, and plastic strain amplitudes versus reversals to failure data, as well as fits determined by the Coffin-Mason equation. As seen in Figure 3.6, the elastic behavior at the strain amplitude of 0.0070 mm/mm is accurately accounted for with the Coffin-Manson elastic fit. The same strain level was poorly matched by the Ramberg-Osgood relationship (see Figure 3.2) because some plasticity was predicted.

The plastic strain-life fit in Figure 3.6 has a very pronounced slope, in part, because of significant cyclic softening at higher strain levels. Due to cyclic softening at higher strain amplitudes, the failure criteria for all of the tests conducted was determined to be final fracture and not crack initiation (or certain load drop). Since in the low cycle fatigue regime (high strain amplitudes), most of the fatigue life is spent in the crack growth stage [16], the short life regime data points are further shifted towards the right as compared to the long life regime data points by considering final fracture rather than crack initiation as the failure criterion. As a result of such shift in the short life regime fatigue data, the resulting ε'_f and c are larger than typical.

The strain-life fatigue data for different strain ratios generated in this study are superimposed in Figure 3.7. It can be seen from this figure that fatigue life is reduced by increasing the R_ε values, specifically in the long life regime. This is expected because negative strain ratios (i.e. R_ε = -1 and R_ε = -0.5) contain relatively smaller mean stresses when compared to the other R_ε values resulting in some tensile mean stresses. As a comparison, fully-reversed tests yield an endurance limit, the strain amplitude at which the life exceeded 1.0E6 cycles without failure, of 0.0050 mm/mm strain amplitude, while

this value reduces to 0.0045 mm/mm strain amplitude for R_ε = -0.5, 0.0040 mm/mm strain amplitude for R_ε = 0, and 0.0030 mm/mm strain amplitude for R_ε = 0.5.

No significant difference in fatigue life was observed at higher strain amplitudes (above 0.0070 mm/mm) when comparing all the data with different strain ratios. This is due to the presence of plastic deformation causing mean stress relaxation, and therefore, a less pronounced effect of R_ε. When the strain amplitude decreased, the influence of a larger R_ε on the fatigue life became greater. The effect of R_ε was mainly observed in R_ε = 0.5 tests, where the fatigue life was greatly reduced as compared to tests with lower strain ratios.

Fractography Analysis

Scanning Electron Microscopy (SEM) was used to characterize the fracture surfaces of the tested specimens and to find inclusions, voids or any material defects at crack initiation sites. The majority of fracture surfaces contained inclusions with an average size of 11 μm at the crack initiation site. The chemical composition of the inclusions was found to be rich in carbon and oxygen content, with these elements making up about 70% of the chemical composition. Titanium, aluminum and vanadium content in the inclusions made less than 4% of the chemical composition.

For fully-reversed fatigue tests at strains above 0.0080 mm/mm, multiple well defined crack initiation sites were present and each initiation was attributed to a cluster of inclusions. An example of this is shown in Figure 3.8(a), for the fully-reversed strain amplitude of 0.0120 mm/mm. The crack propagation area is shown by II in this figure. Four well defined crack initiation sites were observed (denoted by arrows). At the most

pronounced site (red arrow), a cluster of inclusions near the surface was observed, as magnified in Figure 3.8(b). The second dominating crack initiation site is denoted by the yellow arrow and two relatively smaller initiation sites are denoted by the black arrows. The presence of multiple crack initiations sites may be explained by the crack growth stage dominating the fatigue failure process in low cycle regime (i.e. high strain amplitude tests), providing time and opportunity for other cracks to initiate [23,24]. Similar characteristics were observed in tests at different strain ratios.

In another example presented in Figure 3.9(a), where the strain amplitude was 0.0080 mm/mm with R_ε = -1, there is a well-defined crack initiation site on the surface (indicated by the red arrow). There was also another crack initiation site approximately 90° (indicated by the black arrow) from the main initiation site. This site did not fully develop and was most likely arrested by the crack propagation area of the main initiation site. The reason why the main initiation site fully developed, and was the driving flaw that caused final fracture, could be attributed to the number of inclusions found at each site. As seen in Figure 3.9(b), the main crack initiation site had approximately four inclusions near the surface, while the initiation site that was 90° apart, seen in Figure 3.9(c), had only two inclusions.

The number of crack initiation sites reduced to a single, well defined site at lower strain amplitudes for all investigated R_ε values. Figure 3.10(a), for example, presents the fracture surface with a single crack initiation site for a fatigue test with strain amplitude of 0.0060 mm/mm and R_ε = 0. The origination site is enclosed by the red rectangle and indicated by the black arrow. The area indicated by II shows the crack propagation region which ends at the arc shaped region that appears at the bottom tip of the yellow arrow of

area II. The arc indicates the transition from the crack propagation region to final fracture. Figure 3.10(b) offers a close view of the inclusions around the initiation site for the pulsating test at the strain amplitude of 0.0060 mm/mm. Upon close inspection, it is observed that approximately five inclusions at the surface, denoted by the red circles, caused the crack initiation for this specimen.

Comparing Figure 3.10(a) with Figure 3.8(a) shows how the number of crack initiation sites and the maximum stress response may influence the crack propagation and final fracture region. In Figure 3.10(a) the crack propagated to a depth of 2.08 mm from the crack initiation site, and the fracture morphology resembled that of a typical metal fatigue fracture [16]. In Figure 3.8(a), the two dominating crack initiation sites (red and yellow arrow), and the two smaller initiation sites (denoted by the black arrows) propagated independently until they merged leaving a crack propagation region with an overall depth of 2.37 mm from the main initiation site. In Figure 3.8(a), the multiple crack initiation sites caused the crack propagation region to be wider with an area of 8.87 mm^2, while the single crack initiation site in Figure 3.10(a) resulted in a crack propagation region with an area of 5.49 mm^2. On the other hand, the difference in crack propagation area is also in agreement with the effect of maximum stress on the size of the final fracture area; a larger maximum stress, σ_{max} (defined as $\sigma_{max} = \sigma_a + \sigma_m$), typically results in a larger final fracture area, and therefore, a smaller crack growth area. In Figure 3.8, σ_{max} = 723MPa and in Figure 3.10, σ_{max} = 831MPa; thus, resulting in the size of crack growth area and final fracture area in Figure 3.10 to be, respectively, smaller and larger than the ones in Figure 3.8.

In single or multiple crack initiation sites associated with low or high strain level tests, the number of inclusions or imperfections seems to have a major role on the crack development and fatigue life of Ti-6Al-4V ELI. As the number of inclusions, and thus, the size of the cluster of inclusions around the initiation site increased, the specimen's fatigue life was observed to decrease. For example, two fatigue tests conducted at the strain amplitude of 0.0060 mm/mm with R_ε = -1 had a fatigue life difference of 82,658 reversals and each test had one well defined initiation site. The first test, seen in Figure 3.11(a), lasted for 124,952 reversals and contained approximately nine inclusions at the initiation site. The second test, seen in Figure 3.11(b), had a life of 207,610 reversals and approximately four inclusions near the surface where the crack initiated. Further observations also indicate that the number of inclusions has more influence over the fatigue life than the inclusion size. The maximum inclusion size for the specimen in Figure 3.11(a) was 54 μm and the total area of the inclusion cluster was 4,890 μm^2. The fracture surface shown in Figure 3.11(b) contained a relatively large inclusion of 105 μm in size and an overall cluster surface area of 3,719 μm^2. When comparing these two figures, the presence of a large inclusion did not appear to significantly affect the fatigue behavior. However, the overall size of the cluster in Figure 3.11(a) is larger and appears to have a detrimental effect on the fatigue behavior. Therefore, one may conclude that presence of a relatively large cluster of inclusions near surface can significantly impact the fatigue resistance of Ti-6Al-4V ELI.

Across the different R_ε values used, the fracture surfaces presented the same characteristics regarding the number of crack initiation sites and the effect of inclusions. The number of inclusions near the surface and their cluster size were found to have the

most influence on the fatigue behavior of Ti-6Al-4V ELI. The higher the number of inclusions and the larger their cluster size, the shorter the fatigue life. In cases where multiple crack initiation sites were present, the one with most inclusions was dominant, propagating and causing the final failure. Since Ti-6Al-4V ELI is considered to be a ductile behaving material, the final fracture surface exhibits a cup and cone type shape; this in turn results in a slanted shear fracture. This trend was observed in every fracture surface, regardless of strain amplitude or ratio applied. The location of the crack initiation site propagated perpendicularly to the applied load, and as the crack approached the end of the propagation region and changed to final fracture mode, the fracture occurred along a 45° plane.

Table 3.1 Deformation and fatigue properties of Ti-6Al-4V ELI investigated in this study.

Monotonic Properties	**Ti-6Al-4V ELI**
Modulus of elasticity, E (GPa)	106
Yield strength (0.2% offset), σ_y (MPa)	992
Ultimate tensile strength, σ_u (MPa)	1,062
Percent elongation, %EL	15
Percent reduction in area, %RA	47
True fracture strength, $\tilde{\sigma}_{fB}$ (MPa)	1,361
True fracture strain, ε_f (%)	64
Cyclic Properties	
Cyclic modulus of elasticity, E' (GPa)	100
Cyclic strength coefficient, K' (MPa)	780
Cyclic strain hardening exponent, n'	0.017
Fatigue strength coefficient, σ'_f *(MPa)*	1,317
Stress-based fatigue strength coefficient, $\sigma'_{f,\sigma}$ *(MPa)*	805
Fatigue strength exponent, b	-0.060
Stress-based fatigue strength exponent, b_σ	-0.014
Fatigue ductility coefficient, ε'_f	4.83
Fatigue ductility exponent, c	-0.898

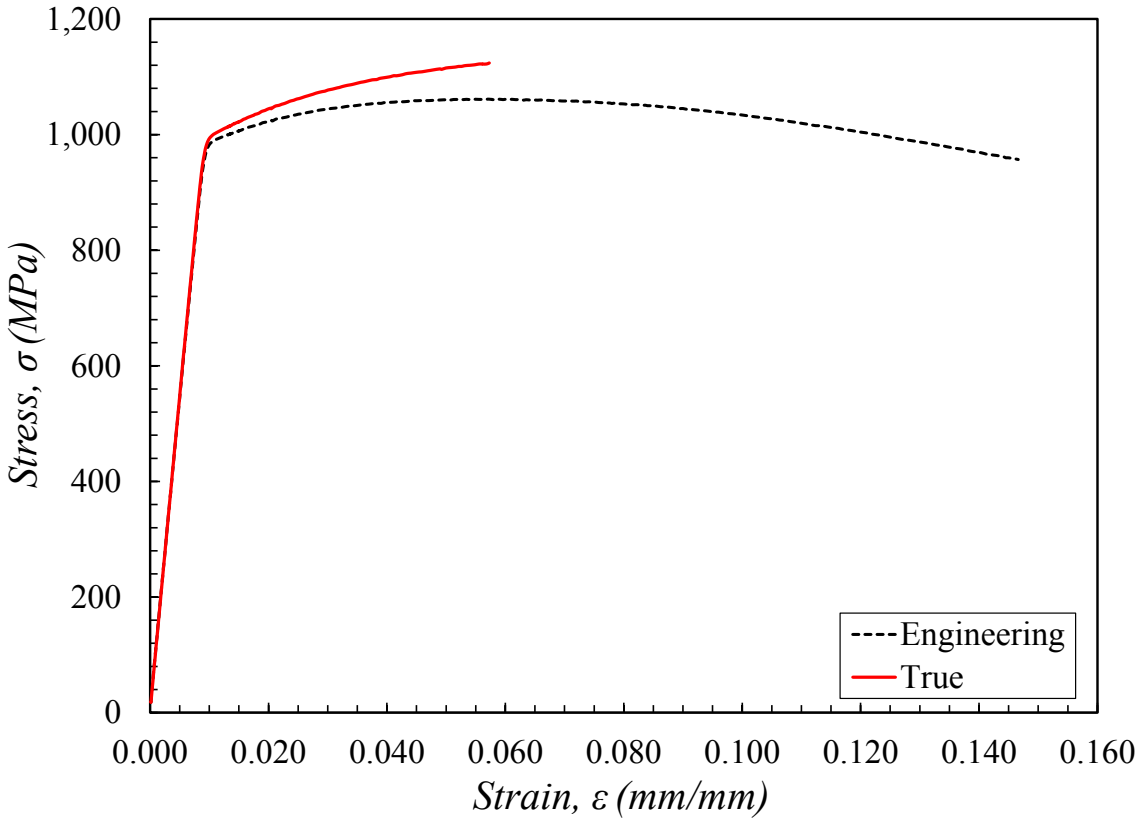

Figure 3.1 Monotonic tension test results of Ti-6Al-4V ELI at 0.001 s^{-1} strain rate.

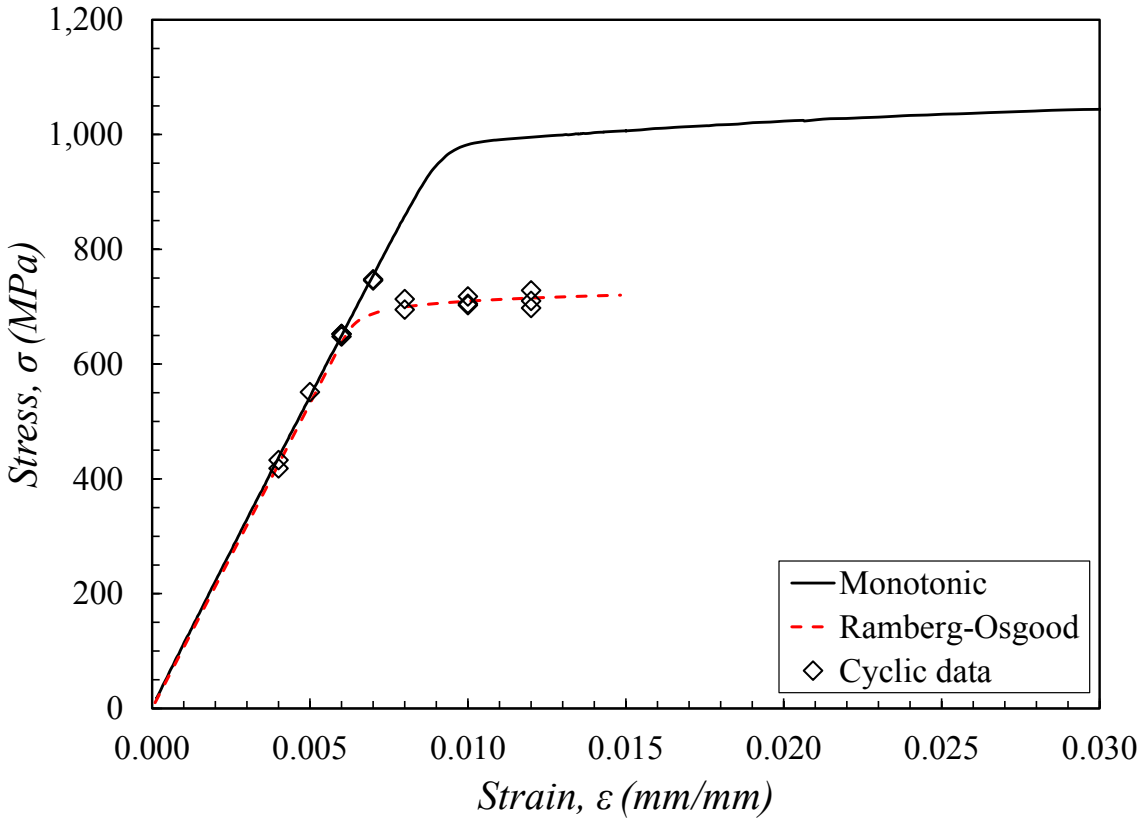

Figure 3.2 Ramberg-Osgood fit superimposed with cyclic deformation data of R_ε= -1 and engineering tensile monotonic test results.

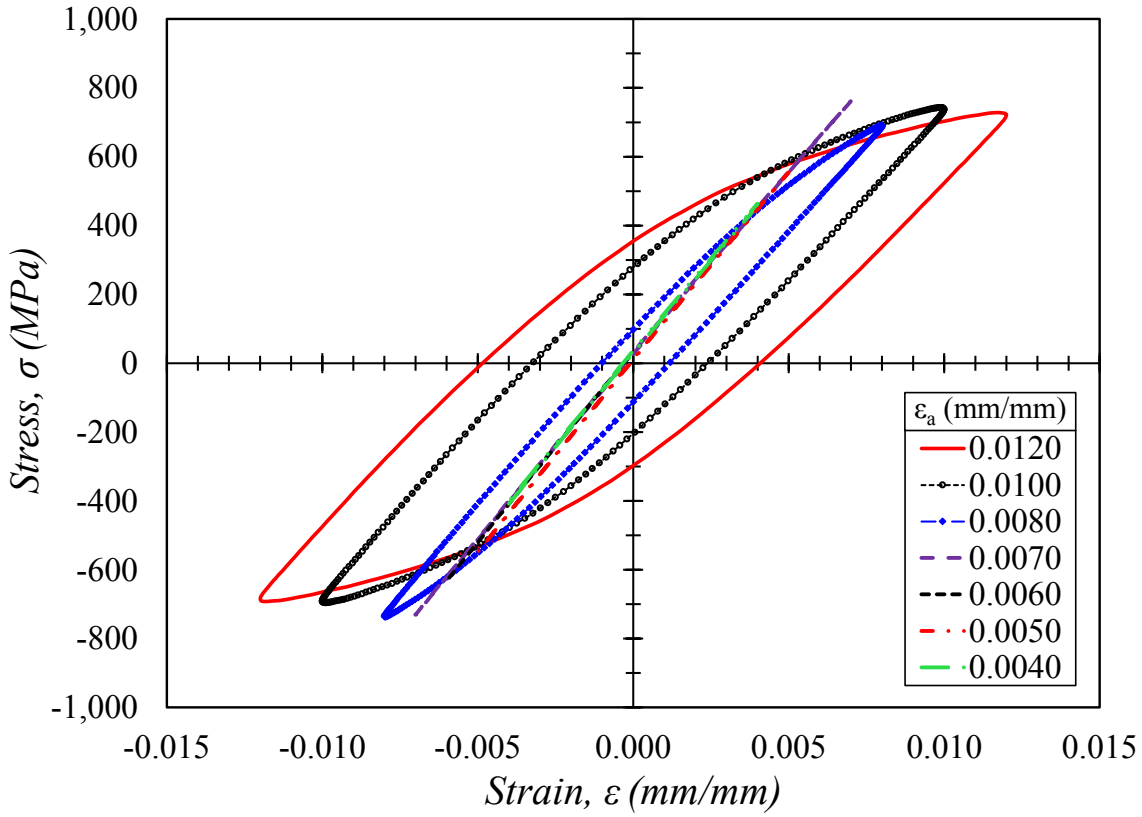

Figure 3.3 Stabilized cycle hysteresis loops for fully-reversed strain-controlled fatigue tests.

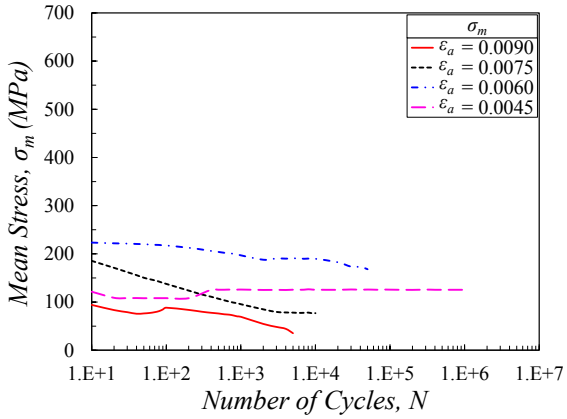

(a)

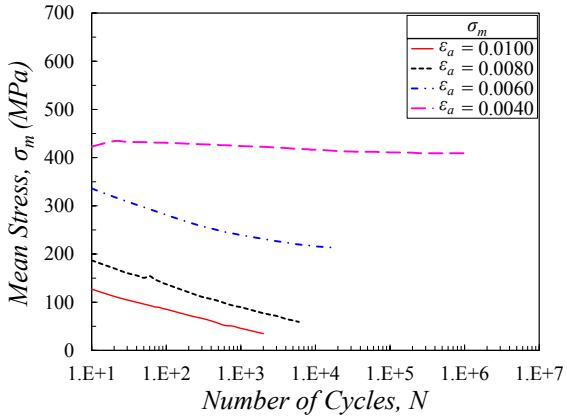

(b)

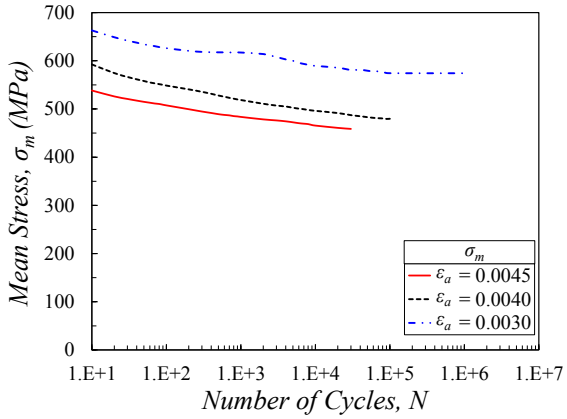

(c)

Figure 3.4 Cyclic mean stress response for strain-controlled mean strain fatigue tests with different R_ε values.

(a) R_ε= -0.5 (tension-compression), (b) R_ε= 0 (tension-release), and (c) R_ε= 0.5 (tension-tension). All strain values are in mm/mm.

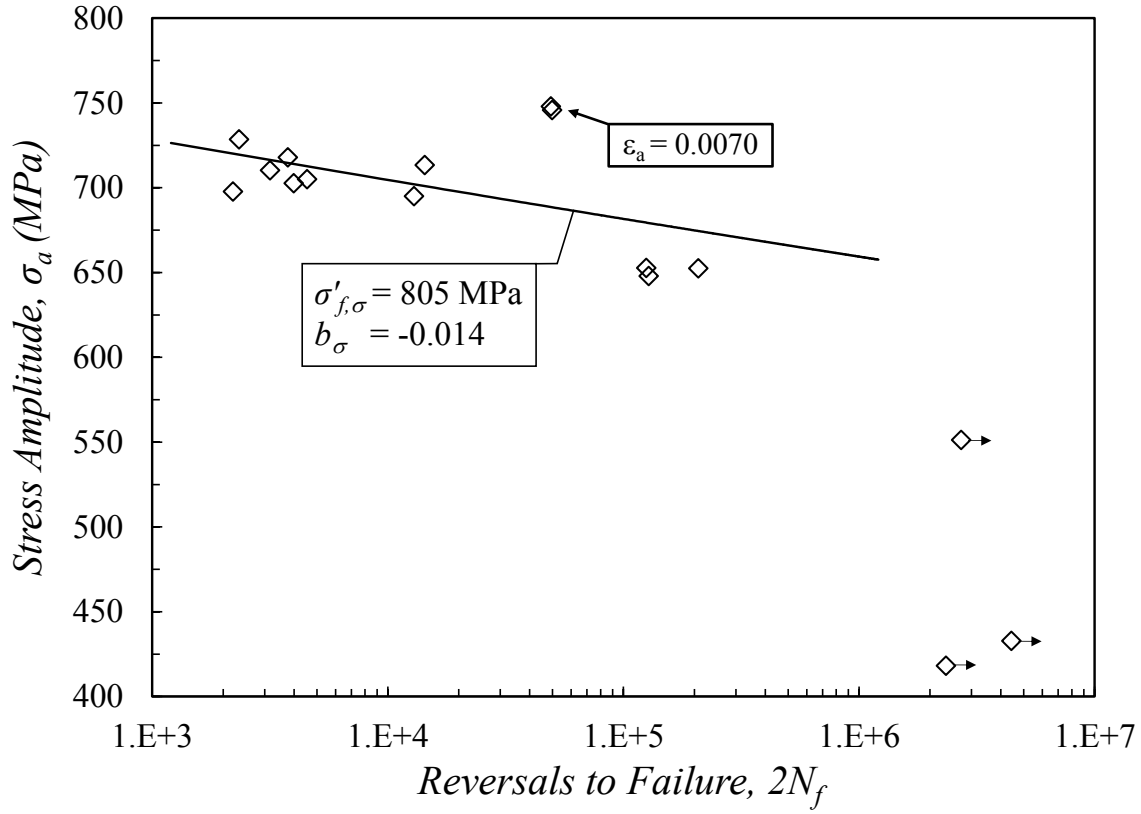

Figure 3.5 Stress-life data and fit of fully-reversed strain-controlled fatigue tests.

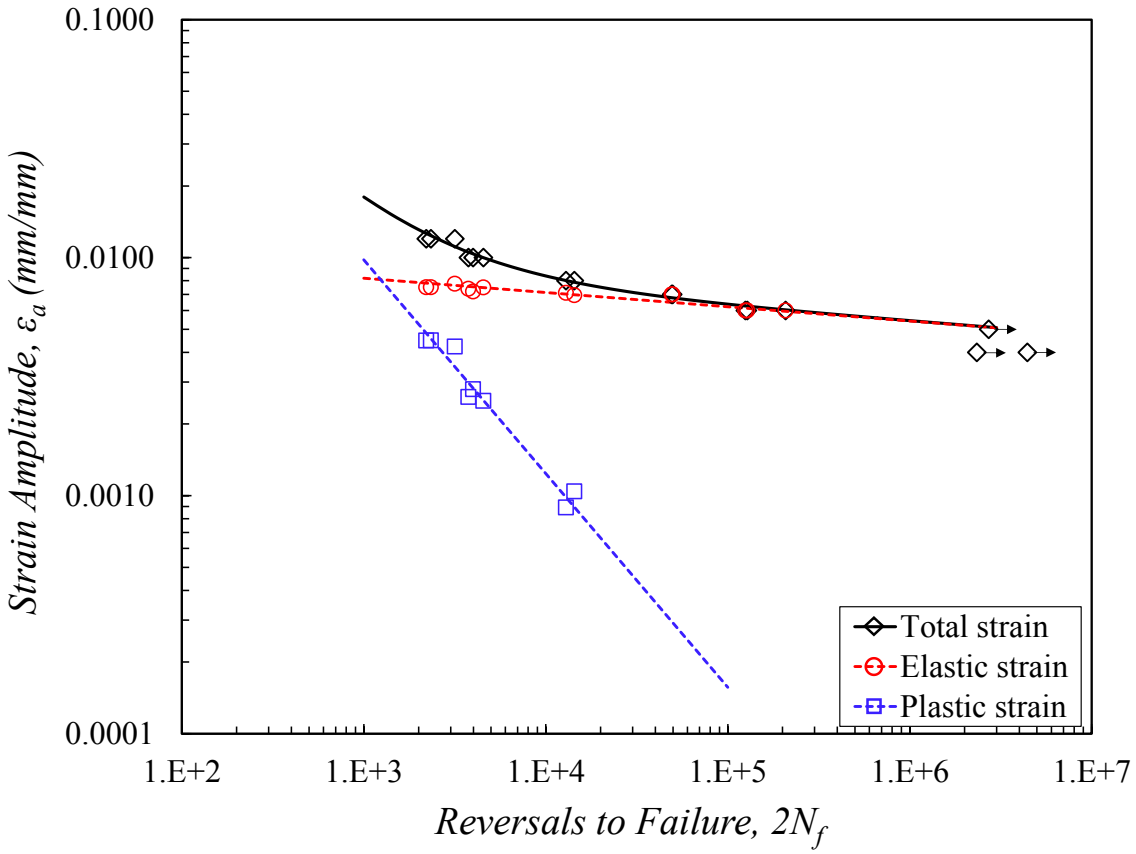

Figure 3.6 Strain-life plot of fully-reversed (R_ε = -1) fatigue data including the corresponding elastic and plastic strain data and fits.

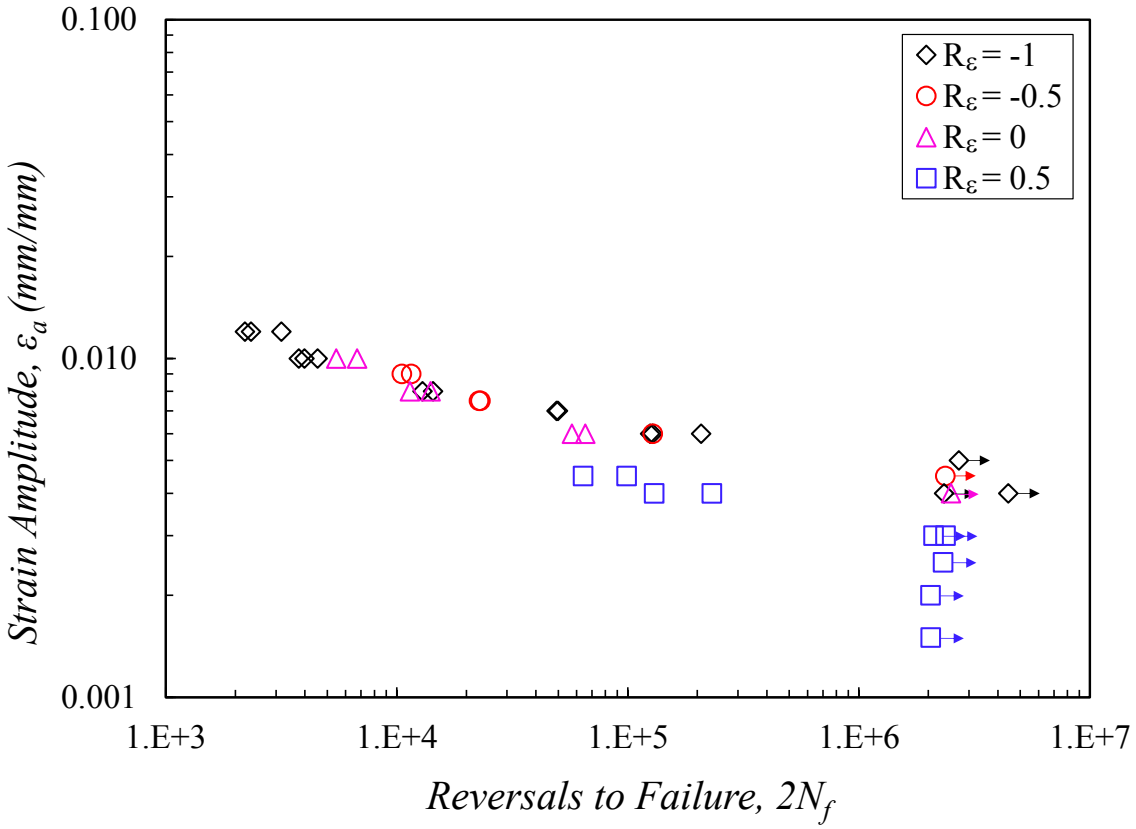

Figure 3.7 Comparison of strain amplitude versus fatigue life data for strain-controlled fatigue tests with different R_ε.

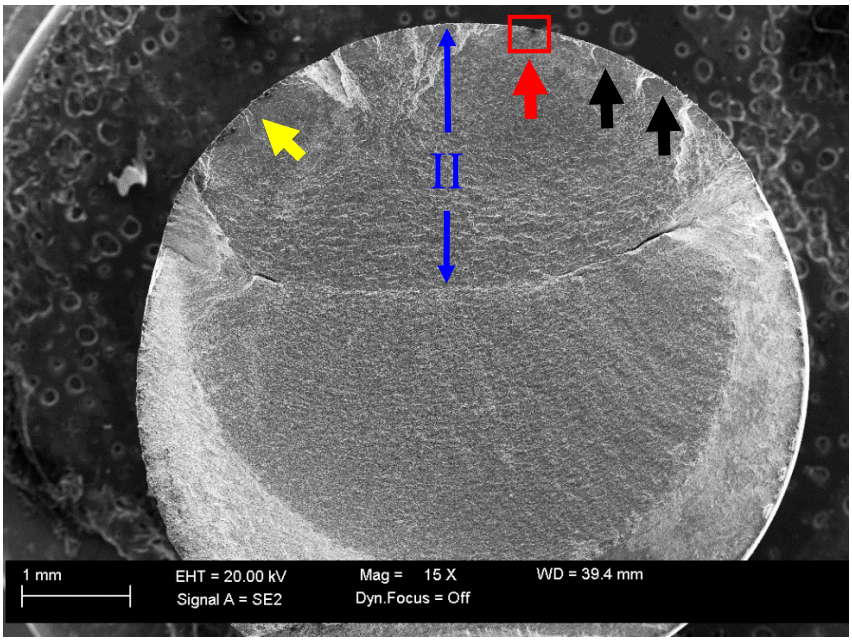

(a)

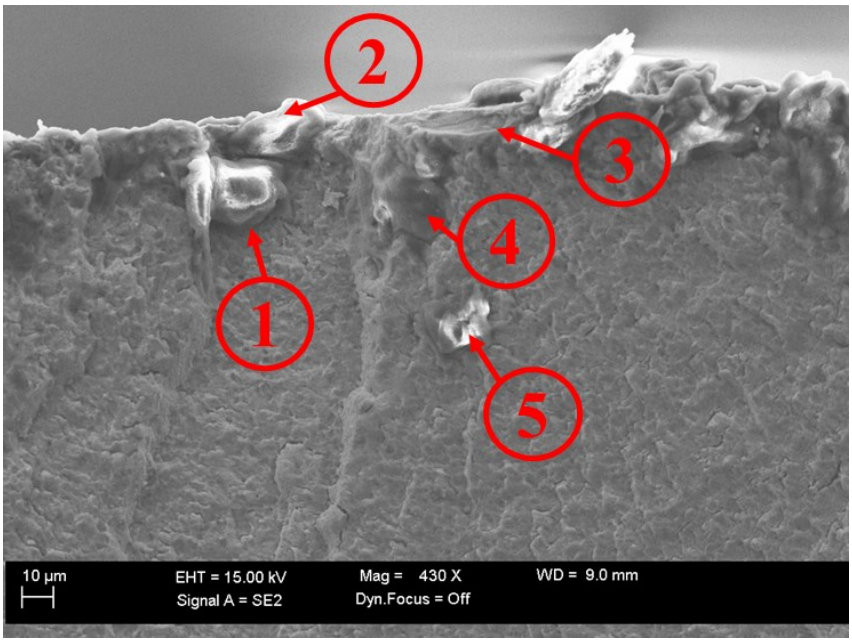

(b)

Figure 3.8 SEM images of a Ti-6Al-4V ELI specimen tested under fully-reversed 0.0120 mm/mm strain amplitude with a life of 2,336 reversals.

(a) Fracture surface and crack initiation sites (arrows show multiple crack initiation sites and II indicates the crack propagation area), and (b) view of the red box indicating a cluster of five inclusions at the main crack initiation site.

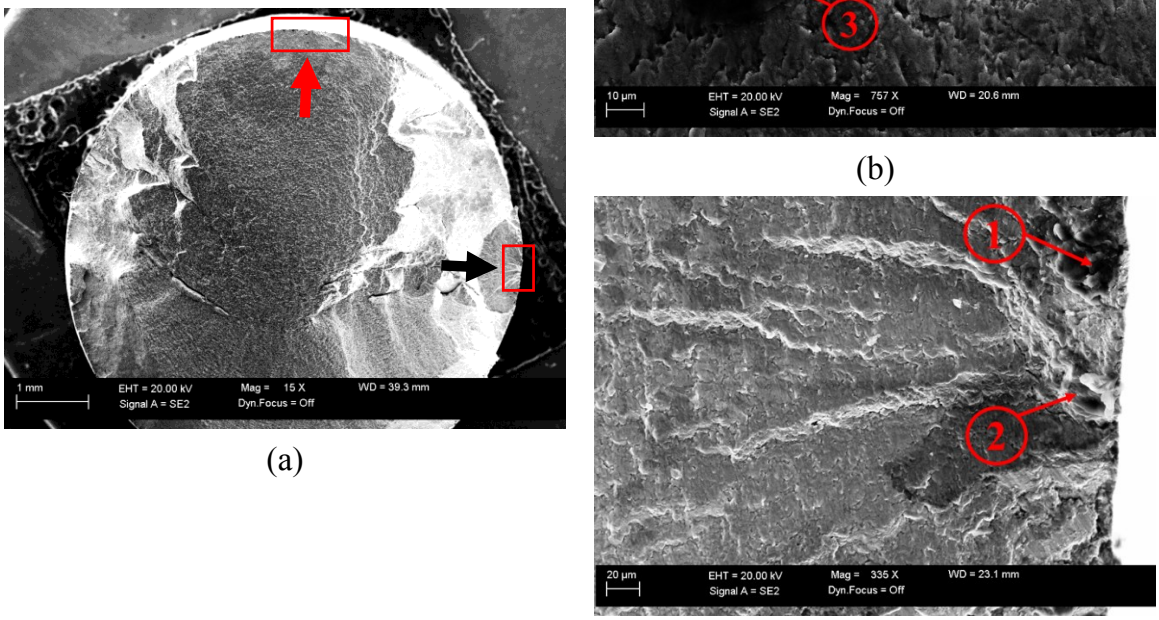

(a)

(b)

(c)

Figure 3.9 SEM images of a Ti-6Al-4V ELI specimen tested under fully-reversed 0.0080 mm/mm strain amplitude with a life of 14,338 reversals.

(a) Fracture surface and crack initiation sites (red arrow shows the predominant crack initiation site and black arrow indicates the smaller initiation site), (b) four inclusions found on the main initiation site, indicated by the red arrow, and (c) two inclusions found on the initiation site, indicated by the black arrow.

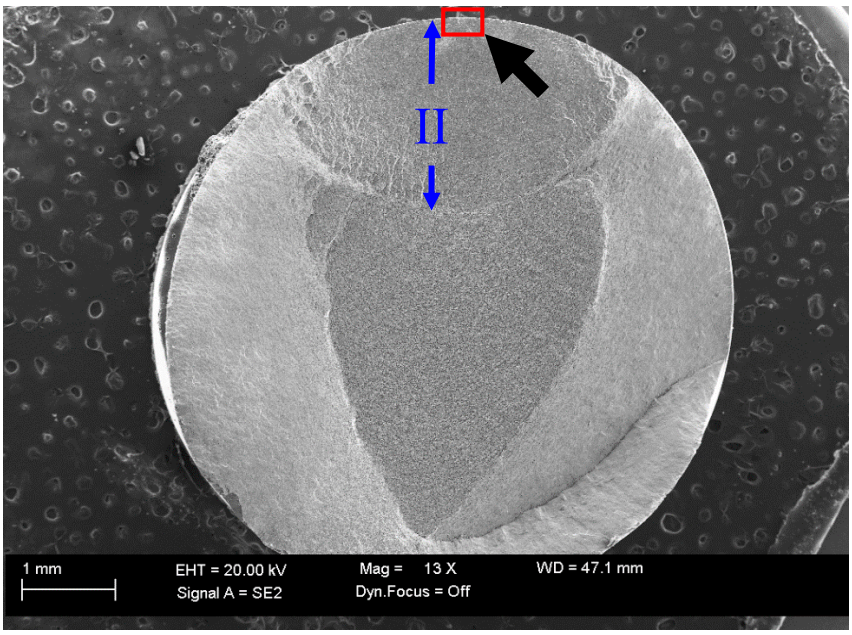

(a)

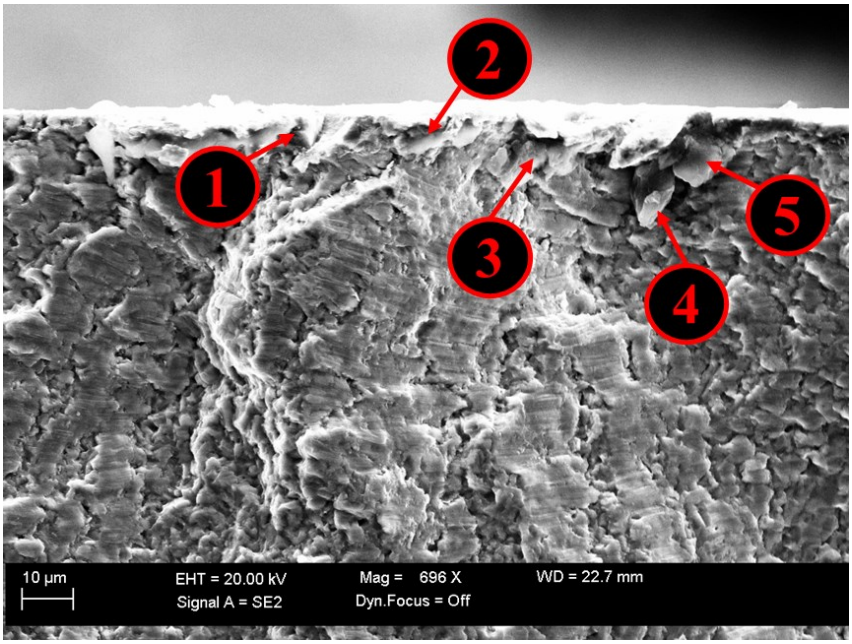

(b)

Figure 3.10 SEM images of a Ti-6Al-4V ELI specimen tested under pulsating 0.0060 mm/mm strain amplitude with a life of 57,292 reversals.

(a) Fracture surface and crack initiation site (black arrow shows a single crack initiation site and II indicates the crack propagation area), and (b) red box enhanced view of the cluster of inclusions found on the crack initiation site.

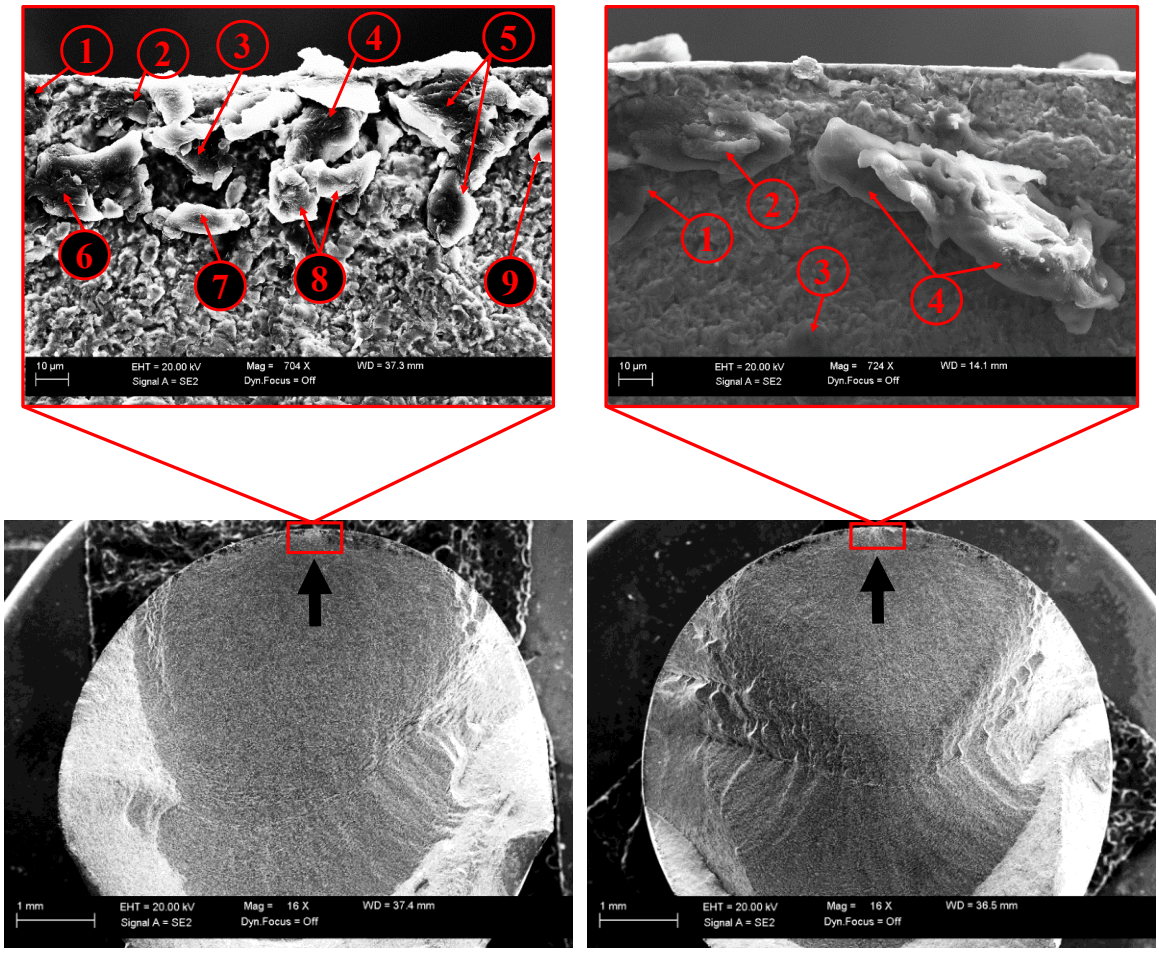

(a) (b)

Figure 3.11 SEM images indicating fracture surface and crack initiation site of two Ti-6Al-4V ELI specimens under fully-reversed 0.0060 mm/mm strain amplitude.

Specimens had a fatigue life of (a) 124,952 reversals, and (b) 207,610 reversals.

CHAPTER IV

MEAN STRESS MODELS

In this chapter, several different models are implemented to account for the effects of mean stress on the fatigue behavior of Ti-6Al-4V ELI. These models are divided into two categories according to the approach that they use. Stress-based models are presented and they include Goodman, Gerber, Morrow, Walker, and Kwofie. Strain-based models include Morrow, Smith-Watson-Topper (SWT), Walker, Kwofie, Ince-Glinka and Modified Smith-Watson-Topper (MSWT).

Stress-Based Models

Some stress-based mean stress models, including Goodman, Gerber, Morrow, Walker, and Kwofie relations, are employed in this study to predict fatigue lives in the presence of mean stresses. Predicted fatigue lives are compared with experimental results to assess the applicability of these models for Ti-6Al-4V ELI. Mean stress parameters used for the stress-life approach are in the form of an equivalent alternating stress versus fatigue life, presented by Eq. (4.1):

$$\sigma_{ar} = f(\sigma_a, \sigma_m) = \sigma'_{f\sigma}\left(2N_f\right)^{b_\sigma} \tag{4.1}$$

where σ_{ar} is considered as an equivalent fully-reversed stress amplitude (as if there was no mean stress, $\sigma_m = 0$), $f(\sigma_a, \sigma_m)$ is a function defined by the employed stress model, $\sigma'_{f,\sigma}$ is the stress-based fatigue strength coefficient, and b_σ is the stress-based fatigue strength

exponent. $\sigma'_{f,\sigma}$, and b_σ were obtained using linear regression on the semi-log plot of the stress amplitude, σ_a, versus reversals to failure, $2N_f$, from fully-reversed strain-controlled tests, previously presented in Figure 3.5(a).

σ_{ar} will vary depending on the parameters used by each of the stress models employed; therefore, σ_{ar} is a general representation and will be denoted by the name of each model. The purpose of the stress models is to offer, for any given combination of stress amplitude, σ_a, and mean stress, σ_m, an equivalent fully-reversed stress amplitude, σ_{ar}, that is estimated to cause the same fatigue damage [25]. Once the equivalent stress amplitude is found, Basquin's relation, expressed by Eq. (4.1), can be used to predict fatigue life.

Goodman

In the Goodman model, presented by Eq. (4.2), σ_a is the stress amplitude, σ_m is the mean stress, and σ_u is the ultimate tensile strength, obtained from monotonic testing.

$$\sigma_{Goodman} = \sigma_{ar} = \frac{\sigma_a}{1-\frac{\sigma_m}{\sigma_u}} \tag{4.2}$$

Fatigue life predictions based on the Goodman model are compared against experimentally observed fatigue lives in Figure 4.1. Scatter bands with a factor of three are given to compare the effectiveness of the models. It is important to note that runouts were included with arrows used to indicate the three possible outcomes. The first outcome; if the arrow is oriented along the solid 45° line, the predicted life was the same as the experimental data, a runout. Second, if the arrow is oriented horizontally, the experimental life was a runout, while the predicted life was finite. In the third case, if the

arrow points vertically, the experimental life was finite, while the predicted life was infinite.

As seen in Figure 4.1, the model performs poorly even for R_ε = -1 data. The scatter observed for R_ε = -1 is due to cyclic softening of the material, causing the stress response of the mid-life stable cycle to yield similar values for strain amplitudes higher than 0.0070 mm/mm, as listed in Table 2.2. In particular, the predicted life corresponding to fully-reversed 0.0070 mm/mm strain amplitude is greatly miscalculated due to the stress amplitude being larger than the ones at higher strains. Since the material does not experience cyclic softening at 0.0070 mm/mm strain amplitude, the stress response is higher, causing the stress-based model to predict significantly shorter fatigue life at this strain amplitude. It is also seen that due to cyclic softening influencing the stress response at strain amplitudes above 0.0070 mm/mm, the model wrongly predicts infinite life for the fully-reversed strain amplitude tests at 0.0060 mm/mm. For tests at R_ε = -0.5, R_ε = 0, and R_ε = 0.5, the Goodman model greatly overestimates the effects of mean stress by predicting shorter fatigue lives than those experimentally observed.

Gerber

In the Gerber model, presented by Eq. (4.3), σ_a is the stress amplitude, σ_m is the mean stress, and σ_u is the ultimate tensile strength obtained from monotonic testing.

$$\sigma_{Gerber} = \sigma_{ar} = \frac{\sigma_a}{1-(\frac{\sigma_m}{\sigma_u})^2} \tag{4.3}$$

The Gerber model is a modified version of the Goodman relation which will predict a reduced effect of mean stress on the fatigue behavior as compared to the Goodman model. Predictions based on the Gerber model are compared against

experimentally observed fatigue lives in Figure 4.2. Similar to the Goodman criterion, the predicted fatigue lives based on the Gerber model were not in good agreement with experimental fatigue lives across all R_ε values tested. For strain amplitudes of 0.0070 mm/mm and higher, the majority of predicted fatigue lives are shorter than experimentally observed ones, indicating that the Gerber model, although not to the extent of the Goodman model, overestimates the effects of mean stress. The fatigue lives, for which the mean stress effect was not overestimated, were predicted close to the upper scatter band of three. However, for the majority of strain amplitudes smaller than 0.0070 mm/mm, the model predicts infinite life despite different strain ratios. For $R_\varepsilon = 0.5$ specifically, the Gerber model underestimates the effects of tensile mean stress by predicting longer fatigue lives for all strain amplitudes tested, while mean stresses are often larger than stress amplitudes at this strain ratio (see Table 2.2).

Morrow

In the stress-based Morrow model, presented by Eq. (4.4), σ_a is the stress amplitude, σ_m is the mean stress, and $\tilde{\sigma}_{fB}$ is the true fracture strength.

$$\sigma_{Morrow} = \sigma_{ar} = \frac{\sigma_a}{1-\frac{\sigma_m}{\tilde{\sigma}_{fB}}} \tag{4.4}$$

The use of the true fracture strength instead of the stress-based fatigue strength coefficient, $\sigma'_{f,\sigma}$, was originally proposed by Morrow The true fracture strength, $\tilde{\sigma}_{fB}$, was derived from monotonic tensile tests and was corrected to account for the triaxial stress state at the necking point by using Bridgman's correction factor [16]. Fatigue life predictions based on the Morrow stress-based model are compared with experimentally observed fatigue lives in Figure 4.3. As seen in this figure, the Morrow model exhibits

the same tendency as the Goodman and Gerber models for fully-reversed data. Again, the reason for the scatter is because the stress response from strain-controlled fatigue tests was used to generate stress-life fatigue parameters, thus the same degree of scatter observed in Figure 3.5 will be present even in fully-reversed data, regardless of the stress-based mean stress model employed. For the remaining R_ε = -0.5, R_ε = 0, and R_ε = 0.5 data, the fatigue lives for strain amplitudes below 0.0060 mm/mm are mainly predicted to be infinite, with the exception of one test at 0.0045 mm/mm strain amplitude with R_ε = 0.5. For higher strain amplitudes, this model overestimates the effects of mean stress and predicts shorter fatigue lives as compared to those experimentally observed. In general, the predicted fatigue lives using the Morrow model were not in good agreement with experimental fatigue lives.

Walker

In the stress-based Walker model, presented by Eq. (4.5), σ_a is the stress amplitude, R_σ is the stress ratio, and γ is Walker's fitting constant [25]. This model is appealing due to its parameter γ, which is adjusted to consider the sensitivity of the material to mean stress. For Ti-6Al-4V, the parameter γ has been found to be 0.5431 [25] and was used in this study.

$$\sigma_{Walker} = \sigma_{ar} = \sigma_a \left(\frac{2}{1-R_\sigma}\right)^{1-\gamma} \tag{4.5}$$

The parameter γ, specific to the Walker model, needs to be calibrated with a minimum of two datasets [25]. The first set can be the fully-reversed data and the second set may include any mean stress data. The approach is described in [25], in which the γ parameter was obtained by conducting a multiple linear regression analysis.

Fatigue life predictions based on the stress-based Walker model are compared with experimentally observed fatigue lives in Figure 4.4. As observed in this figure, the Walker model exhibits the same scatter as the previous models for fully-reversed data. For the remaining R_ε = -0.5, R_ε = 0, and R_ε = 0.5 data, the predicted lives are similar to those of Morrow's, indicating the same trend with respect to strain amplitudes below 0.0060 mm/mm being predicted infinite. For higher strain amplitudes, the Walker model also overestimates the effects of mean stress. As a result, the model predicts shorter fatigue lives as compared to those experimentally observed.

Kwofie

In the Kwofie stress-based model [26], presented by Eq. (4.6), σ_a is the stress amplitude, σ_m is the mean stress, α is the mean stress sensitivity parameter, and σ_u is the ultimate tensile strength.

$$\sigma_{Kwofie} = \sigma_{ar} = \sigma_a e^{\left[\alpha\left(\frac{\sigma_m}{\sigma_u}\right)\right]} \tag{4.6}$$

The parameter α will vary depending on the materials sensitivity to mean stress. As presented by Kwofie, α = 0 implies the material is not sensitive to mean stress, while α >0 indicates the sensitivity of the material to mean stress. In this study a value of α = 0.7 was selected for Ti-6Al-4V ELI as it provided the best fatigue life data correlation. Predictions based on Kwofie stress-based model are compared against experimentally observed fatigue lives in Figure 4.5. Similar to the previous models, the predicted fatigue lives based on the stress-based Kwofie model were not in good agreement with experimental fatigue lives across all R_ε values considered in this study. The same trend was observed for the fully-reversed data. For R_ε = -0.5 and 0, strain amplitudes of 0.0060

mm/mm and higher, the predicted lives are shorter than experimentally observed ones, and the fatigue lives for strain amplitudes below 0.0060 mm/mm are predicted to be infinite. For $R_\varepsilon = 0.5$, the Kwofie model predicts longer fatigue lives, thus underestimating the effects of tensile mean stress on fatigue behavior of Ti-6Al-4V ELI.

In conclusion, the stress-based mean stress models considered in this study could not predict fatigue lives accurately for Ti-6Al-4V ELI. The detrimental effect of tensile mean stress is overestimated at higher strain amplitudes, while it is underestimated at lower strain amplitudes using this stress-based mean stress models. The poor predictions obtained from the stress-based models may be explained by the fact that the stress-based fatigue parameters were obtained using the stress response from strain-controlled fatigue tests. However, among the five stress-based models employed, Gerber appears to consider the effects of mean stress somewhat better than the other models.

Strain-Based Models

In this section, different strain-based fatigue life prediction models incorporating mean stress effects are compared to assess their applicability for Ti-6Al-4V ELI. The predicted fatigue lives using strain-based Morrow, Smith-Watson-Topper (SWT), Walker, Kwofie, Ince-Glinka and Modified Smith-Watson-Topper (MSWT) models are compared with experimentally observed fatigue lives.

Morrow

In the Morrow model, given in Eq. (4.7), the mean stress, σ_m, only affects the elastic portion of the Coffin-Mason equation. This is justified by assuming a negligible effect of mean stress in the presence of plastic strain in the low cycle fatigue regime

because of mean stress relaxation. Meanwhile, at lower strain amplitudes, the driving component is the elastic strain and the mean stress may not fully relax; thus, exhibiting a higher influence on the fatigue life [16] .

$$\varepsilon_a = \frac{\sigma_f' - \sigma_m}{E}\left(2N_f\right)^b + \varepsilon_f'\left(2N_f\right)^c \quad (4.7)$$

Fatigue life predictions based on the Morrow approach are compared with experimentally observed fatigue lives in Figure 4.6. As seen from this figure, the fatigue life predictions for the different strain ratios are mostly well within the scatter bands of three with $R^2 = 0.94$. When compared to the stress-based models, presented in Figures 4.1 - 4.5, the strain-based Morrow model is able to effectively reduce the scatter observed for $R_\varepsilon = 0$, - 0.5, and 0.5. Although predictions are within scatter bands of three (with exception of one data point), they all fall closer to the lower bound. This indicates that the Morrow approach is slightly overestimating the effects of mean stress, resulting in slightly conservative fatigue life predictions. For example, as seen in Figure 4.6, four data points that resulted in an experimental runout were predicted to have finite lives by this model. The more accurate fatigue life predictions obtained using the strain-based Morrow approach may be explained by the fact that this approach very well represents the Ti-6Al-4V ELI behavior observed; negligible effect of mean stress in the presence of plastic strain in the low cycle fatigue regime (higher strains) because of mean stress relaxation and more effect of mean stress in high cycle fatigue regime (lower strains) due to the lack of plastic deformation and less mean stress relaxation.

Smith-Watson-Topper (SWT)

The Smith-Watson-Topper (SWT) model is based on strain-life data obtained from fully-reversed tests employing the elastic/plastic coefficients/exponents from the Coffin-Manson relationship (i.e. σ'_f, b, ε'_f, c), presented in Eq. (3.5) . The SWT model is expressed by Eq. (4.8), ε_a is the strain amplitude and σ_{max} is the maximum stress, $\sigma_{max} = \sigma_a + \sigma_m$, where σ_a is the stress amplitude and σ_m is the mean stress [27]. This model takes into account the effects of stress amplitude, as well as mean stress by incorporating σ_{max} into the left hand side of Eq. (3.5).

$$\varepsilon_a \sigma_{max} = \frac{\left(\sigma'_f\right)^2}{E}\left(2N_f\right)^{2b} + \sigma'_f \varepsilon'_f \left(2N_f\right)^{b+c} \tag{4.8}$$

Fatigue life predictions based on the SWT model are compared with experimentally observed fatigue lives in Figure 4.7. Similar to the Morrow approach, the SWT model predicted fatigue lives fairly well within the scatter bands of three, except for two data points. The R^2 between predicted and experimental data for the SWT model is 0.86. Nevertheless, unlike Morrow model, the SWT approach presents a better data distribution around the prediction line.

Walker

In the strain-based Walker model, presented by Eq. (4.9) [25], the $2N_w$ is the equivalent fully-reversed fatigue life, $2N_f$ is the expected fatigue life, R_σ is the stress ratio, γ is the Walker fitting constant, and b is the fatigue strength exponent.

$$2N_w = 2N_f \left(\frac{1-R_\sigma}{2}\right)^{(1-\gamma)/b} \tag{4.9}$$

The approach employed to incorporate the Walker model into strain-based fatigue analysis is proposed in [25] and has been recently employed in [28]. The basis of the

approach is to relate the strain amplitude to an equivalent fully-reversed fatigue life, which is defined by the mean stress model employed (i.e. Walker). The procedure involves combining the Coffin-Mason relationship (Eq. (3.5)) with the mean stress model employed (in this case Eq. (4.9)), thus yielding Eq. (4.10):

$$\varepsilon_a = \frac{\sigma_f'}{E}(2N_w)^b + \varepsilon_f'(2N_w)^c \tag{4.10}$$

This model has been demonstrated to provide reasonable results across a variety of ferrous and non-ferrous metals under cyclic loading with mean strain/stress conditions, such as carbon steels, stainless steels, aluminums, and titanium alloys [25,29]. The parameter γ in the strain-based Walker model is the same as the one employed in the stress-based approach, $\gamma = 0.5431$, as it is considered to be a material constant [25].

The fatigue life prediction capabilities of the Walker model for Ti-6Al-4V ELI under various strain ratios are assessed in Figure 4.8. The Walker model provided fairly good correlations for all the strain ratios considered in this study. However, the Walker model did not offer an improvement over the previously presented strain-based models. The R^2 between predicted and experimental data for the Walker model is 0.86. As seen in Figure 4.8 for $R_\varepsilon = 0$, - 0.5, and 0.5, the Walker model provided similar results as the SWT model. Which can be explained by $\gamma = 0.5431$ being very close to 0.5, a case where Walker is similar to SWT[25]. When comparing Figure 4.7 and 4.8, it was observed that the Walker model is slightly more conservative than SWT, as the predicted fatigue lives were closer to the lower scatter band. Even though the Walker model uses an additional parameter, obtained by fitting non-zero mean stress fatigue data, there was no improvement when compared to SWT. Furthermore, one disadvantage of the Walker model is the fact that it requires having a minimum of two datasets to calibrate γ. While

fully-reversed strain-life data may be commonly accessible, mean strain data are not often readily available.

Kwofie

In the Kwofie model, given in Eq. (4.11), the $2N_k$ is the equivalent fully-reversed fatigue life, $2N_f$ is the expected fatigue life, α is the material sensitivity to mean stress, σ_m is the mean stress, σ_u is the ultimate tensile strength, and b is the fatigue strength exponent.

$$2N_k = 2N_f e^{\left[-\alpha\left(\frac{\sigma_m}{\sigma_u}\right)\right]/b} \tag{4.11}$$

Similar to the strain-based Walker model, the strain amplitude is related to an equivalent fully-reversed fatigue life by using Eq. (4.12), which is based on the Kwofie mean stress model, presented by Eq. (4.11) [25,26]. The parameter α in the strain-based Kwofie model is considered to be the same as the one employed in the stress-based approach, $\alpha = 0.7$.

$$\varepsilon_a = \frac{\sigma_f'}{E}(2N_k)^b + \varepsilon_f'(2N_k)^c \tag{4.12}$$

Fatigue life predictions based on the Kwofie model under various strain ratios are compared against experimentally observed fatigue lives in Figure 4.9. It can be seen from this figure that the strain-based Kwofie model, yielding $R^2 = 0.83$, did not offer an improvement over the previous strain-based approaches. By comparing the fatigue life predictions of Kwofie (Figure 4.9), and Walker (Figure 4.8), for $R_\varepsilon = 0$, and $R_\varepsilon = -0.5$, it is observed that both models, despite Kwofie being an exponential function, offer similar results and the fatigue life predictions are closer to the lower scatter band (i.e. more conservative predictions). The main difference between the Kwofie and Walker models is

for $R_\varepsilon = 0.5$, where the life predictions for Kwofie deviate further from perfect prediction line toward the upper scatter band (i.e. more non-conservative predictions).

Ince-Glinka (I-G)

The Ince-Glinka (I-G) model [30] is combination of the Morrow and the SWT strain-based models. As previously mentioned, in Morrow, the mean stress, σ_m, only affects the elastic portion of the Coffin-Manson equation (Eq. (3.5)) by assuming negligible effect of mean stress in the presence of plastic strain due to mean stress relaxation; therefore, in the I-G model, the SWT correction is applied only to the elastic strain amplitude, $\Delta\varepsilon_e/2$, in Eq. (3.5). In the I-G model, given by Eq. (4.13), $\varepsilon_{a,eq}$ is the equivalent strain amplitude, $\Delta\varepsilon_{e,eq}/2$ is the equivalent elastic strain amplitude, $\Delta\varepsilon_p/2$ is the plastic strain amplitude, σ_{max} is maximum stress, and σ'_f, b, ε'_f, c are the elastic/plastic coefficients/exponents from the Coffin-Manson relationship.

$$\varepsilon_{a,eq} = \frac{\Delta\varepsilon_{e,eq}}{2} + \frac{\Delta\varepsilon_p}{2} = \left(\frac{\sigma_{max}}{\sigma'_f}\right)\frac{\Delta\varepsilon_e}{2} + \frac{\Delta\varepsilon_p}{2} = \frac{\sigma'_f}{E}\left(2N_f\right)^{2b} + \varepsilon_f{}'\left(2N_f\right)^{c} \qquad (4.13)$$

Fatigue life predictions based on the I-G model are compared with experimentally observed fatigue lives in Figure 4.10. As seen from this figure, the fatigue life predictions for the different strain ratios are mostly within the scatter bands of three with $R^2 = 0.91$. In comparison to the fatigue life predictions of Morrow (Figure 4.6), which were observed to be conservative and with $R^2 = 0.94$, the I-G presents a better distribution around the prediction line. Also, the fatigue life predictions of the I-G model offer an improvement over the SWT (Figure 4.7) with $R^2 = 0.86$, while retaining a similar distribution around the prediction line.

Modified Smith-Watson-Topper

The Modified Smith-Watson-Topper (MSWT) model [31], is a revised version of the SWT (Eq. (4.8)) model that incorporates the Walker fitting constant, γ (γ = 0.5431 in this study). The MSWT model is given by Eq. (4.14), where γ is the Walker fitting constant, ε_a is the strain amplitude, σ_{max} is the maximum stress, and σ'_f, b, ε'_f, c are the elastic/plastic coefficients/exponents from the Coffin-Manson relationship. The MSWT model is equivalent to the SWT model when γ = 0.5, because as previously mentioned in the strain-based Walker model and as [31] indicates, when γ = 0.5 the Walker is similar to SWT model.

$$2\gamma\varepsilon_a\sigma_{max} = \frac{\left(\sigma'_f\right)^2}{E}\left(2N_f\right)^{2b} + \sigma'_f\varepsilon'_f\left(2N_f\right)^{b+c} \tag{4.14}$$

The fatigue life predictions of the MSWT model are compared to the experimentally observed fatigue lives in Figure 4.11. The MSWT model provided fairly good correlations for all the strain ratios considered, and it was also observed that the results were mostly conservative. When comparing the MSWT model (Figure 4.11) to the SWT (Figure 4.7), and the Walker model (Figure 4.8), a similar trend was observed for the fatigue life predictions for R_ε = 0, and R_ε = - 0.5; while for R_ε = 0.5 the MSWT model presented better results. The R^2 between predicted and experimental data for the MSWT is 0.86, this is the same R^2 that the SWT and Walker model obtained; therefore, the MSWT model did not offer an improvement over the aforementioned models.

Previously it was mentioned that the γ parameter was obtained by fitting non-zero mean stress fatigue data [25], and since this type of fatigue data is not readily available, it presented a drawback on the applicability of the Walker model. However, [31] proposed

a new method that uses monotonic tensile properties (often available) for any given material to calculate γ. The method for determining the Walker fitting constant is given by Eq. (4.15), where σ_u is ultimate tensile strength, and σ_y is yield strength.

$$\gamma = 0.5 \pm \frac{\sigma_u - \sigma_y}{\sigma_u + \sigma_y} \tag{4.15}$$

This method greatly simplifies the calculation γ, and it offers suitable results when compared to the procedure given in [25]. Employing Eq. (4.15), with the monotonic tensile properties of Ti-6Al-4V ELI found in this study, resulted in the same γ parameter value of 0.5431.

In conclusion, the Morrow model with $R^2 = 0.94$ surpasses the SWT, Walker, Kwofie, I-G, and MSWT models for accounting for the mean strain effect on the fatigue behavior of Ti-6Al-4V ELI, as evident by comparing Figure 4.6 with Figures 4.7 - 4.11. The I-G model fairly accurately predicted the fatigue lives, as seen in Figure 4.10 with $R^2 = 0.91$, and provided a better overall data distribution in comparison to the Morrow, SWT, Walker, Kwofie or MSWT model. Unlike the SWT, Walker, Kwofie, and I-G model, the effects of mean stress are slightly overestimated by the Morrow and MSWT models, and all the data points fell close to, or under the prediction line. While several different models have been proposed to adjust for mean stress effects (i.e. Walker, Kwofie, MSWT) and claimed to offer an improvement [25,26,31] over typical approaches such as Morrow and SWT, they did not provide better results for Ti-6Al-4V ELI fatigue data in this study.

Some final remarks about the strain-based mean stress correction models; the I-G was the only model capable of surpassing the results obtained with the SWT model. The Morrow was found to be the most efficient and accurate of the six correction models

used, although it demonstrated a tendency to overestimate mean stress effects. The better fatigue life predictions obtained using this approach can be explained by the model assuming a negligible effect of mean stress in the presence of plastic strain in the low cycle fatigue regime because of mean stress relaxation. This model considers a higher influence of mean stress on the fatigue life at lower strain amplitudes (high cycle fatigue regime), where the driving component is elastic strain and mean stress may not fully relax. This very well represents the Ti-6Al-4V ELI behavior observed in this study, with full mean stress relaxation in the low cycle fatigue regime (higher strains) and partial mean stress relaxation and more effect of mean stress in high cycle fatigue regime (lower strains).

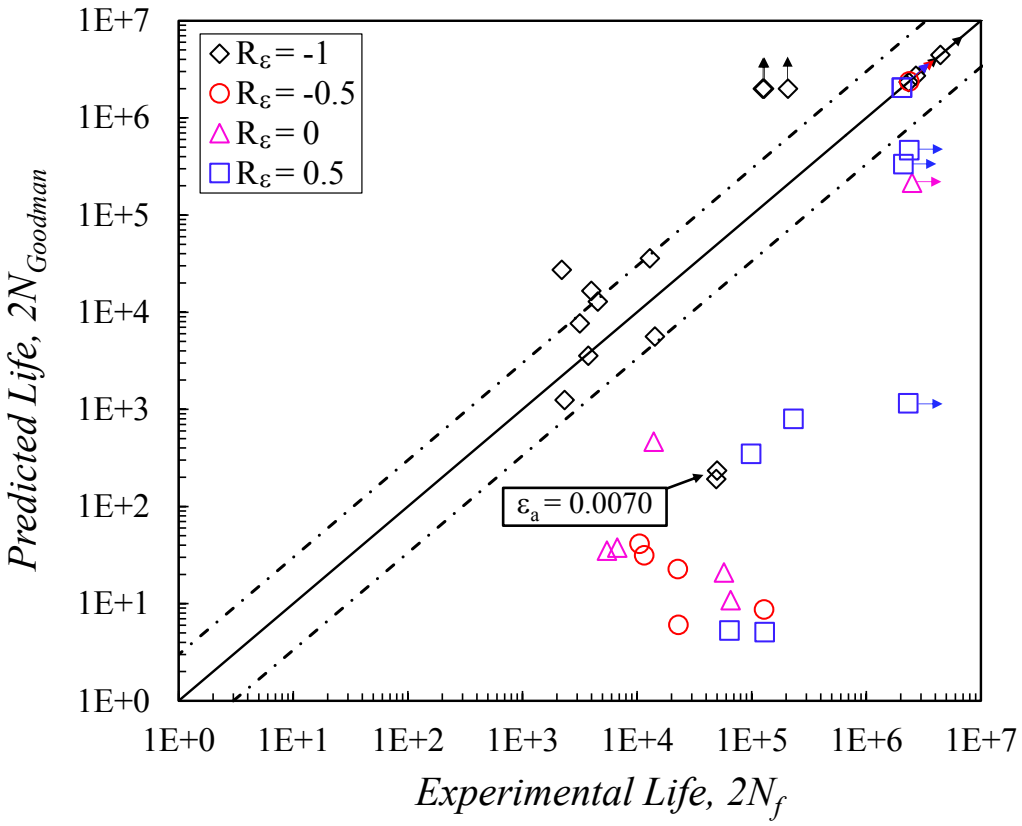

Figure 4.1 Fatigue life predictions, using Goodman stress-based model, compared with experimentally obtained fatigue lives.

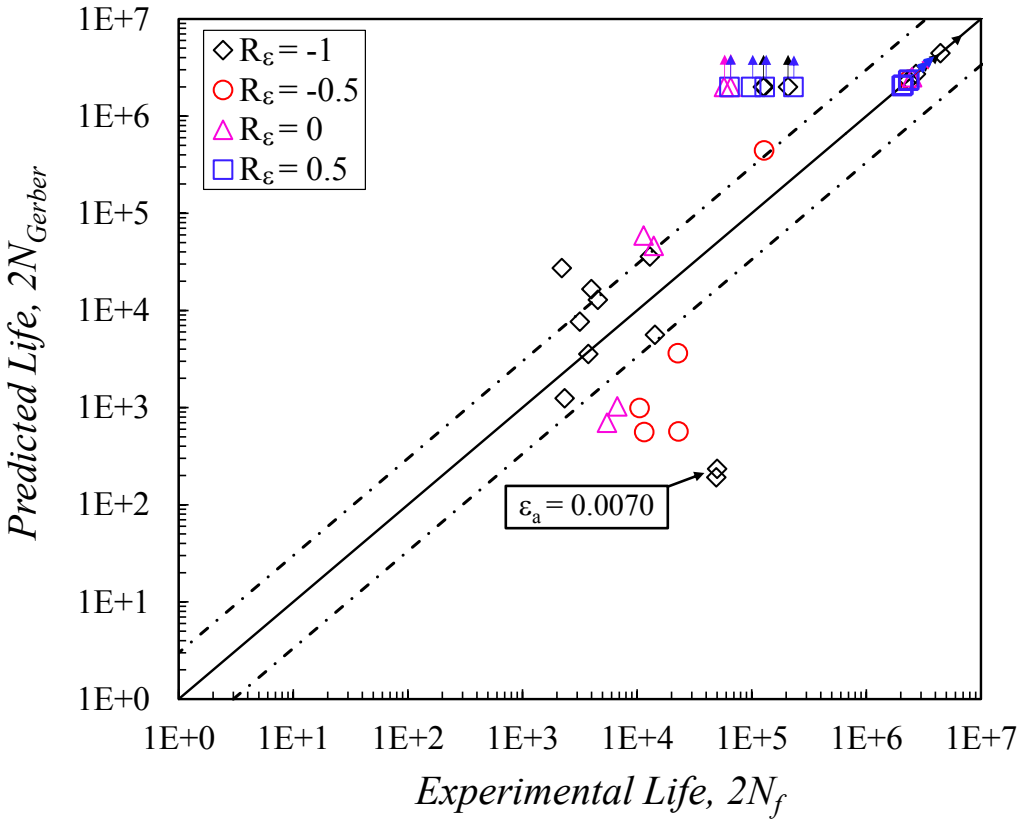

Figure 4.2 Fatigue life predictions, using Gerber stress-based model, compared with experimentally obtained fatigue lives.

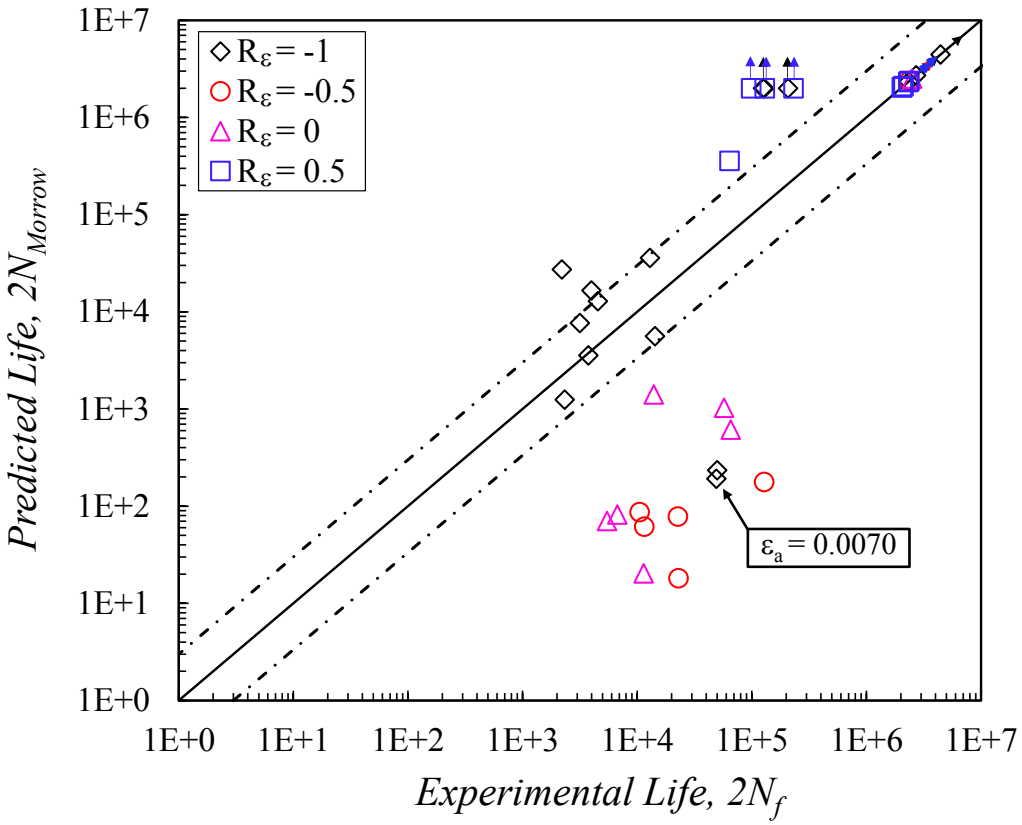

Figure 4.3 Fatigue life predictions, using Morrow stress-based model, compared with experimentally obtained fatigue lives.

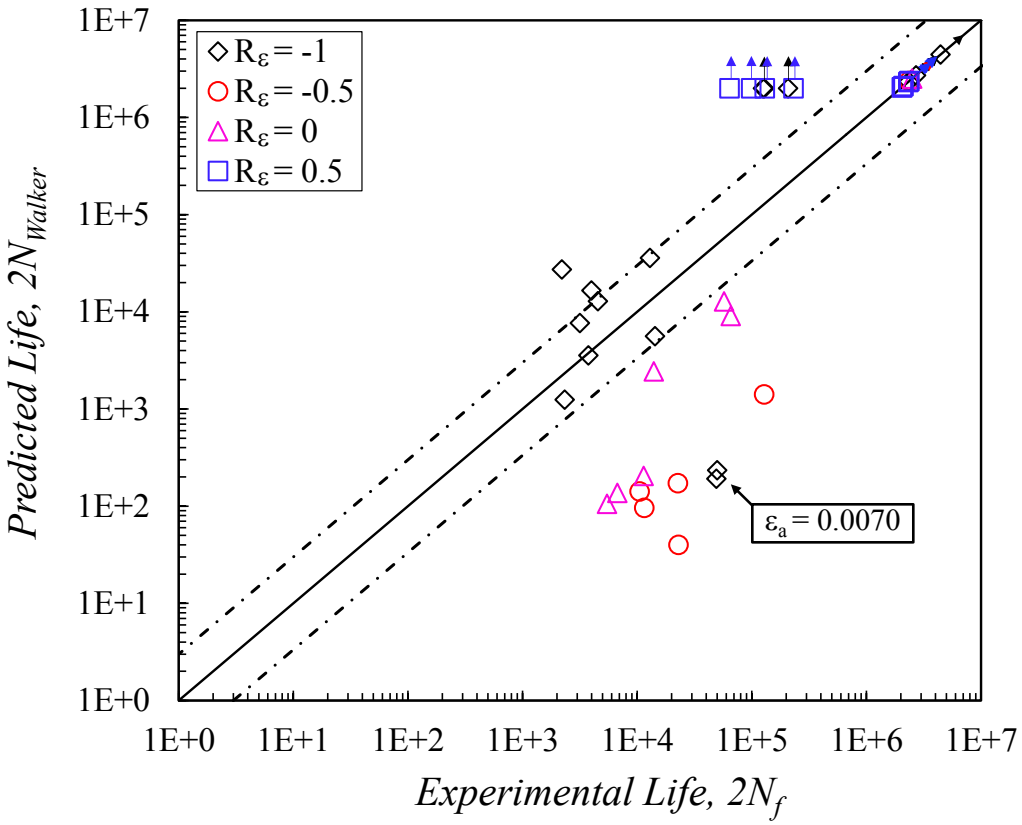

Figure 4.4 Fatigue life predictions, using Walker stress-based model, compared with experimentally obtained fatigue lives.

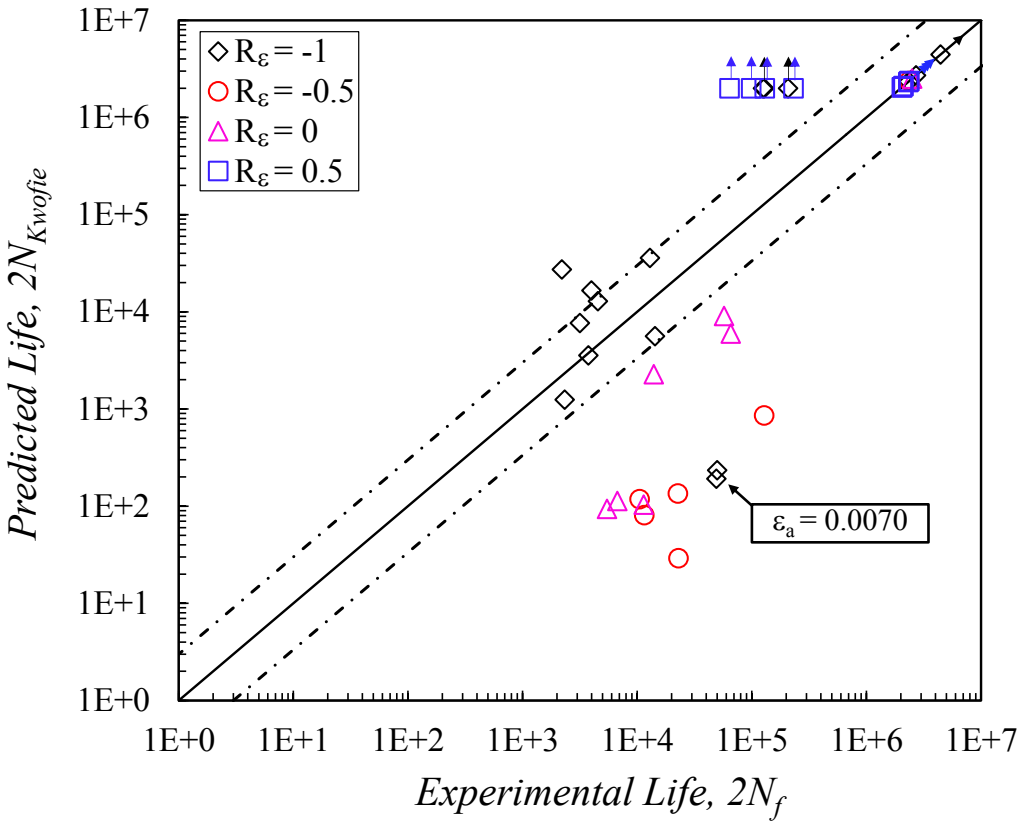

Figure 4.5 Fatigue life predictions, using Kwofie stress-based model, compared with experimentally obtained fatigue lives.

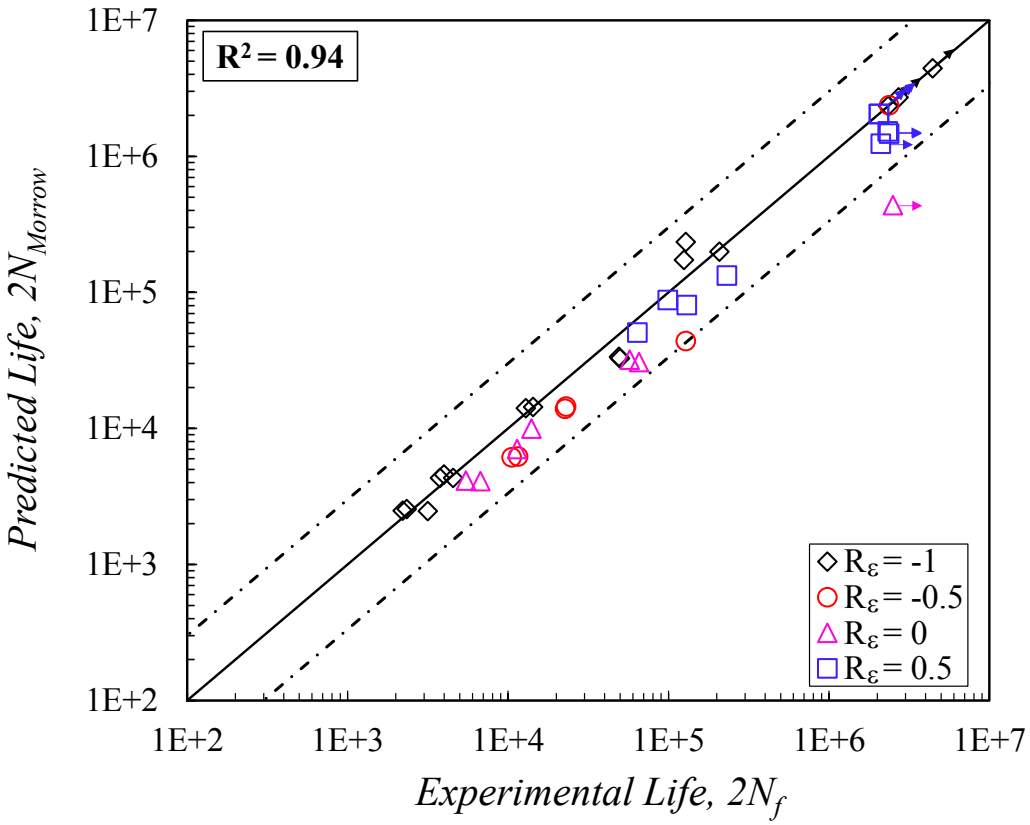

Figure 4.6 Fatigue life predictions, using Morrow strain-based model, compared with experimentally obtained fatigue lives.

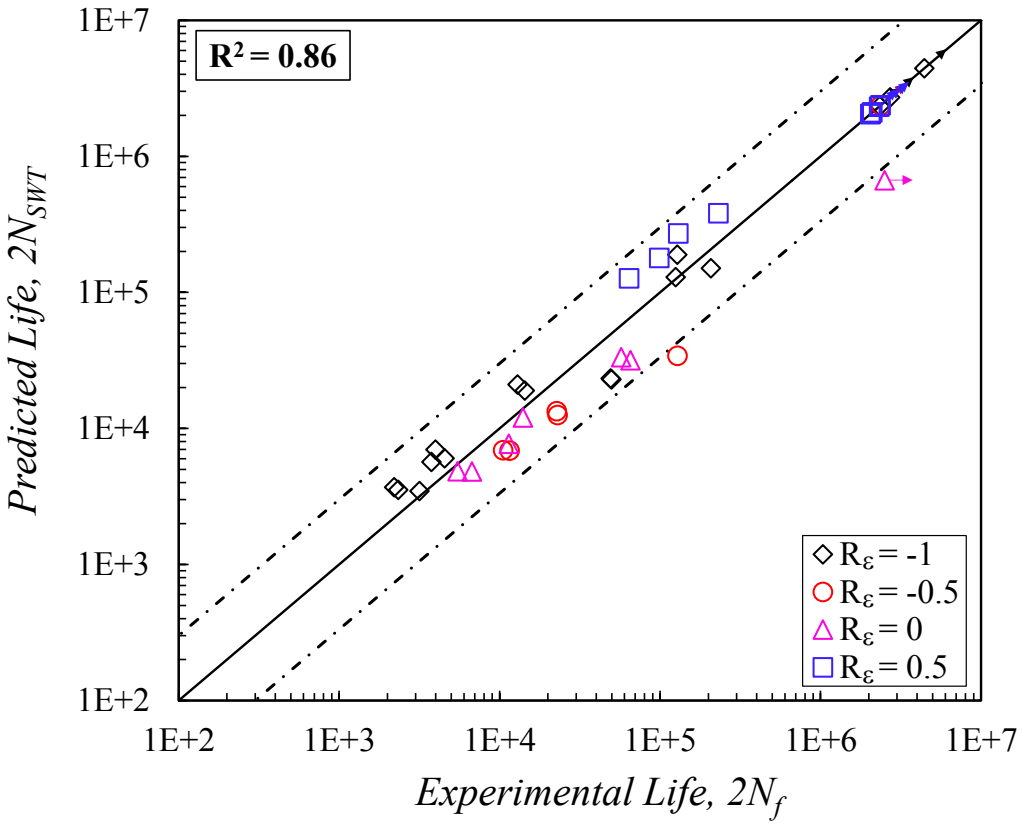

Figure 4.7 Fatigue life predictions, using Smith-Watson-Topper (SWT) strain-based model, compared with experimentally obtained fatigue lives.

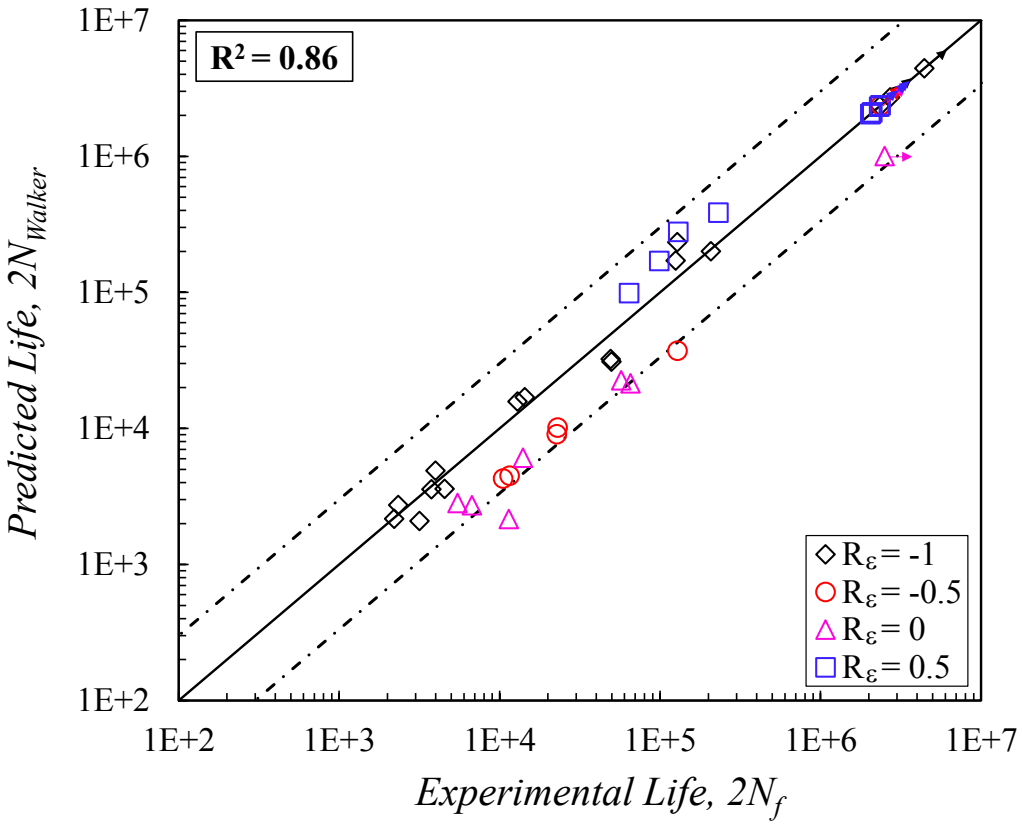

Figure 4.8 Fatigue life predictions, using Walker strain-based model, compared with experimentally obtained fatigue lives.

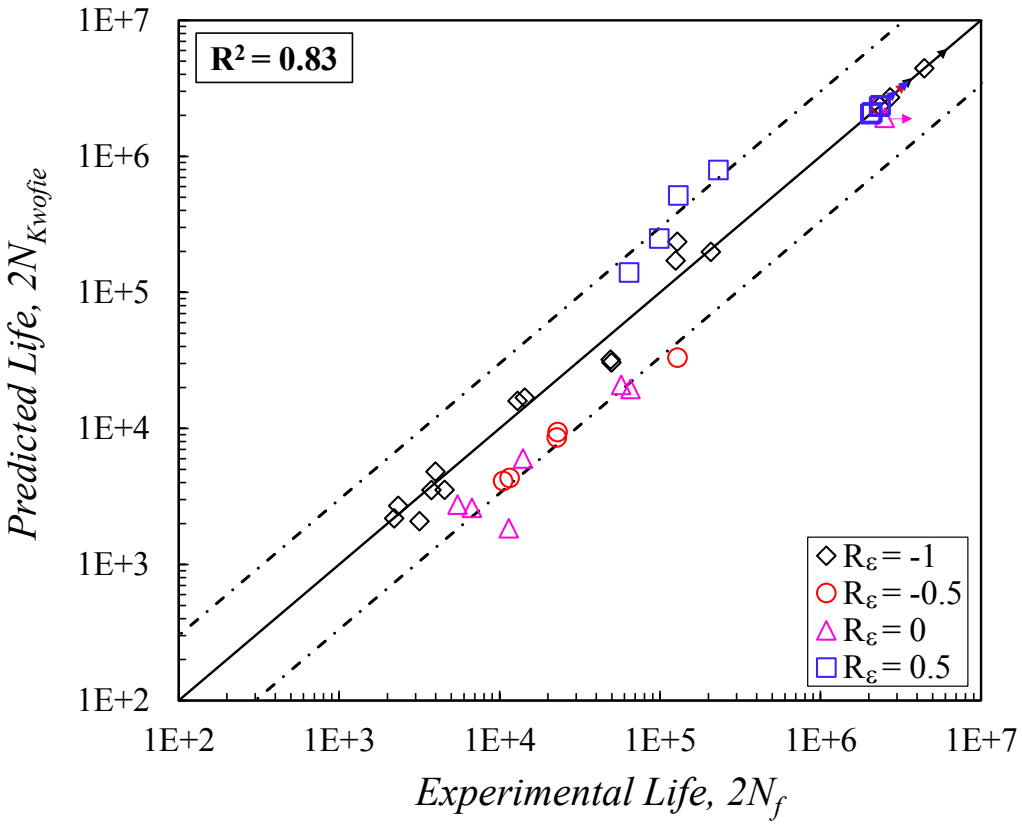

Figure 4.9 Fatigue life predictions, using Kwofie strain-based model, compared with experimentally obtained fatigue lives.

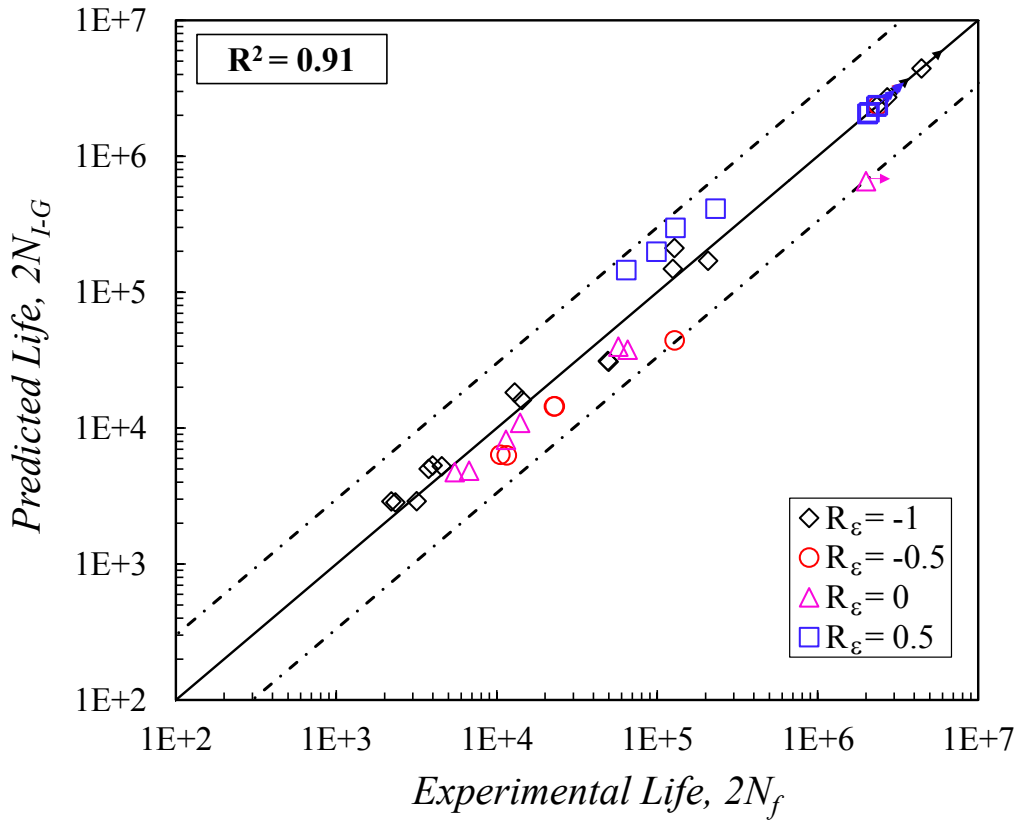

Figure 4.10 Fatigue life predictions, using Ince-Glinka (I-G) strain-based model, compared with experimentally obtained fatigue lives.

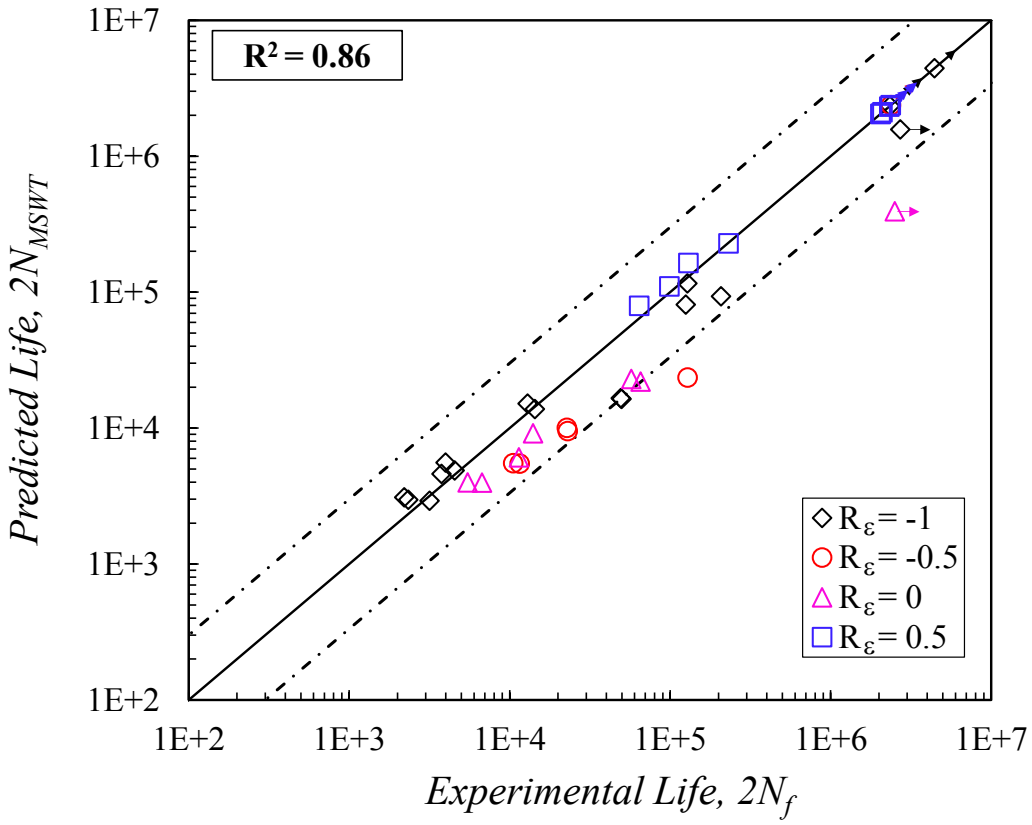

Figure 4.11 Fatigue life predictions, using Modified Smith-Watson-Topper (MSWT) strain-based model, compared with experimentally obtained fatigue lives.

CHAPTER V

CONCLUSIONS

This study investigated the fatigue behavior of Ti-6Al-4V ELI with and without mean strain. The ability of several stress-based and strain-based models to account for mean stress effects was also evaluated. The following conclusions can be drawn from the experimental results and analysis:

1. Ti-6Al-4V ELI exhibited a low level of strain hardening under tensile monotonic loading. Once the stress surpassed 960 MPa, as the proportional limit, the stress only slightly increased until it reached the ultimate tensile strength. The amount of cyclic hardening observed for fully-reversed cyclic stress-strain behavior of Ti-6Al-4V ELI was also very small, having a cyclic strength exponent of $n' = 0.017$.
2. The presence of cyclic softening in Ti-6Al-4V ELI was observed only when plastic deformation was present (strain amplitudes above 0.0070 mm/mm). It is also important to emphasize that for strain amplitudes above 0.0070 mm/mm, the stress amplitude reduced to a value of 700 MPa as the stress response stabilized. Regardless of strain amplitude, the stress response was relatively constant in the presence of plastic deformation.

3. At strain amplitudes near the yield point, cyclic plastic strain deformation was introduced as a result of accumulation of localized plastic deformation. For example, at a strain amplitude of 0.0080 mm/mm, the initial hysteresis loop indicated no plastic deformation, while plastic deformation was observed in the stabilized cycle hysteresis loop.
4. Mean strains had more effect on fatigue life in the high cycle regime, where mean stress relaxation was minimal. In the low cycle regime, where the mean stress almost fully relaxed, no effect of mean strain on fatigue life was observed. This indicates mean strain has no effect of fatigue behavior of Ti-6Al-4V ELI in the absence of mean stress.
5. The strain ratio of $R_\varepsilon = 0.5$ was the most damaging one in this study. Strain amplitudes tested with this strain ratio were below the endurance limit for the fully-reversed condition, yet the fatigue lives decreased significantly as a result of the mean stress being present.
6. Fatigue failure for Ti-6Al-4V ELI was found to initiate at the surface, where several inclusions facilitated the crack initiation. The number of inclusions near the surface and their cluster size were found to have the most influence on the fatigue behavior of this titanium alloy. The overall cluster size presented greater influence than the size of inclusions.

7. Fractography analysis revealed several crack initiation sites at relatively large strain amplitudes, while only a single initiation site was observed at lower strains. In cases where multiple crack initiation sites were present, the one with most inclusions (thus, having the larger cluster size) dominated.
8. Stress-life prediction methods were not successful in capturing the influence of mean stress, even for fully-reversed data. This could be in part due to the fact that strain-controlled data was used to generate stress-life fatigue parameters in this study.
9. The strain-based prediction models for mean stress effects yielded better results in comparison to the stress-based methods because they could account for the presence of plastic deformation, cyclic softening and mean stress relaxation observed in Ti-6Al-4V ELI.
10. While the Morrow strain-based model exhibited a tendency to slightly overestimate the effects of mean stress, it was found to be the most reliable in predicting the fatigue behavior of Ti-6Al-4V ELI in the presence of mean strain/stress. The Ince-Glinka model provided a better balance by predicting conservative and non-conservative fatigue lives. The Smith-Watson-Topper, Walker, Kwofie, and Modified Smith-Watson-Topper models also provided reasonable fatigue life predictions; however, the Walker and Kwofie models require having a minimum of two datasets to determine their adjustable mean stress parameters (i.e. γ and α).

REFERENCES

[1] Sha W, Malinov S. Titanium alloys: modelling of microstructure, properties and applications. Elsevier; 2009.

[2] Donachie MJ. Titanium: a technical guide. 2nd ed. ASM International; 2000.

[3] Joshi VA. Titanium alloys: an atlas of structures and fracture features. CRC Press; 2006.

[4] Akahori T, Niinomi M. Fracture characteristics of fatigued Ti–6Al–4V ELI as an implant material. Materials Science and Engineering: A 1998;243:237–43. doi:10.1016/S0921-5093(97)00807-1.

[5] Saitova LR, Höppel HW, Göken M, Semenova IP, Valiev RZ. Cyclic deformation behavior and fatigue lives of ultrafine-grained Ti-6AL-4V ELI alloy for medical use. International Journal of Fatigue 2009;31:322–31. doi:10.1016/j.ijfatigue.2008.08.007.

[6] Niinomi M. Mechanical properties of biomedical titanium alloys. Materials Science and Engineering: A 1998;243:231–6. doi:10.1016/S0921-5093(97)00806-X.

[7] Wang K. The use of titanium for medical applications in the USA. Materials Science and Engineering: A 1996;213:134–7. doi:10.1016/0921-5093(96)10243-4.

[8] Bian L, Thompson SM, Shamsaei N. Mechanical properties and microstructural features of direct laser-deposited Ti-6Al-4V. JOM 2015;67:629–38. doi:10.1007/s11837-015-1308-9.

[9] Peters M, Hemptenmacher J, Kumpfert J, Leyens C. Structure and properties of titanium and titanium alloys. In: Leyens C, Peters nfred, editors. Titanium and Titanium Alloys, Wiley-VCH Verlag GmbH & Co. KGaA; 2003, p. 1–36.

[10] Akahori T, Niinomi M, Fukunaga K-I. An investigation of the effect of fatigue deformation on the residual mechanical properties of Ti-6Al-4V ELI. Metall and Mat Trans A 2000;31:1937–48. doi:10.1007/s11661-000-0221-0.

[11] ASTM F136-13. Standard specification for wrought Titanium-6Aluminum-4Vanadium ELI (extra low interstitial) alloy for surgical implant applications (UNS R56401). ASTM International: West Conshohocken, PA; 2013.

[12] Lin C-W, Ju C-P, Chern Lin J-H. A comparison of the fatigue behavior of cast Ti–7.5Mo with c.p. titanium, Ti–6Al–4V and Ti–13Nb–13Zr alloys. Biomaterials 2005;26:2899–907. doi:10.1016/j.biomaterials.2004.09.007.

[13] Williams JC. Titanium. 2nd ed. Berlin, Heidelberg: Springer Berlin Heidelberg; 2007.

[14] Tan C, Li X, Sun Q, Xiao L, Zhao Y, Sun J. Effect of α-phase morphology on low-cycle fatigue behavior of TC21 alloy. International Journal of Fatigue 2015;75:1–9. doi:10.1016/j.ijfatigue.2015.01.010.

[15] Wu GQ, Shi CL, Sha W, Sha AX, Jiang HR. Effect of microstructure on the fatigue properties of Ti–6Al–4V titanium alloys. Materials & Design 2013;46:668–74. doi:10.1016/j.matdes.2012.10.059.

[16] Stephens RI, Fatemi A, Stephens RR, Fuchs HO. Metal fatigue in engineering. John Wiley & Sons; 2000.

[17] Shamsaei N, Gladskyi M, Panasovskyi K, Shukaev S, Fatemi A. Multiaxial fatigue of titanium including step loading and load path alteration and sequence effects. International Journal of Fatigue 2010;32:1862–74. doi:10.1016/j.ijfatigue.2010.05.006.

[18] ASTM E606/E606M-12. Standard test method for strain-controlled fatigue testing. ASTM International: West Conshohocken, PA; 2012.

[19] ASTM E112-13. Standard test methods for determining average grain size. ASTM International: West Conshohocken, PA; 2013.

[20] ASTM E8 / E8M-15a. Standard test methods for tension testing of metallic materials. ASTM International: West Conshohocken, PA; 2015.

[21] Carrion PE, Shamsaei N. Strain-based fatigue data for Ti–6Al–4V ELI under fully-reversed and mean strain loads. Data in Brief 2016;7:12–5. doi:10.1016/j.dib.2016.02.014.

[22] Takao K, Kusukawa K. Low-cycle fatigue behavior of commercially pure titanium. Materials Science and Engineering: A 1996;213:81–5. doi:10.1016/0921-5093(96)10226-4.

[23] Shamsaei N, Fatemi A. Small fatigue crack growth under multiaxial stresses. International Journal of Fatigue 2014;58:126–35. doi:10.1016/j.ijfatigue.2013.02.002.

[24] Shamsaei N. Multiaxial fatigue and deformation including non-proportional hardening and variable amplitude loading effects. University of Toledo, 2010.

[25] Dowling NE. Mean stress effects in strain–life fatigue. Fatigue & Fracture of Engineering Materials & Structures 2009;32:1004–19. doi:10.1111/j.1460-2695.2009.01404.x.

[26] Kwofie S. An exponential stress function for predicting fatigue strength and life due to mean stresses. International Journal of Fatigue 2001;23:829–36. doi:10.1016/S0142-1123(01)00044-5.

[27] Smith, K. N., Watson, P., Topper, T. H. A stress-strain function for the fatigue of metals. Journal of Materials, JMLSA 1970;5:767–78.

[28] Mahtabi MJ, Shamsaei N. An energy-based approach for fatigue life prediction of NiTi in presence of tensile mean strain and stress. Submitted for Publication 2016.

[29] Dowling NE, Calhoun CA, Arcari A. Mean stress effects in stress-life fatigue and the Walker equation. Fatigue & Fracture of Engineering Materials & Structures 2009;32:163–79. doi:10.1111/j.1460-2695.2008.01322.x.

[30] Ince A, Glinka G. A modification of Morrow and Smith–Watson–Topper mean stress correction models. Fatigue & Fracture of Engineering Materials & Structures 2011;34:854–67. doi:10.1111/j.1460-2695.2011.01577.x.

[31] Lv Z, Huang H-Z, Wang H-K, Gao H, Zuo F-J. Determining the Walker exponent and developing a modified Smith-Watson-Topper parameter model. Journal of Mechanical Science and Technology 2016;30:1129–37. doi:10.1007/s12206-016-0217-3.